

Linking Macroscopic and Nanoscopic Ionic Conductivity: A Semiempirical Framework for Characterizing Grain Boundary Conductivity in Polycrystalline Ceramics

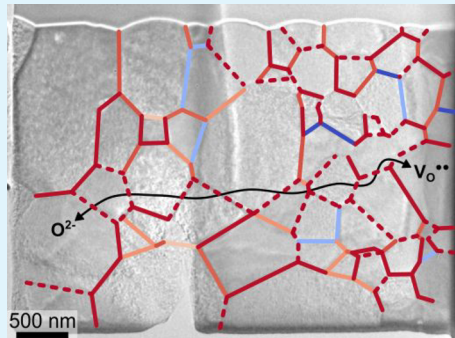
William J. Bowman,*†^{ID} Amith Darbal,[‡] and Peter A. Crozier*^{*,†}^{ID}

[†]School for Engineering of Matter, Transport and Energy, Arizona State University, 501 E. Tyler Mall, Tempe, Arizona 85287-6106, United States

[‡]Nanomegas USA, 1095 W. Rio Salado Pkwy #110, Tempe, Arizona 85281, United States

Supporting Information

ABSTRACT: Understanding the chemical and charge transport properties of grain boundaries (GBs) with high point defect concentrations (beyond the dilute solution limit) in polycrystalline materials is critical for developing ion-conducting solids for electrochemical energy conversion and storage. Elucidation and optimization of GBs are hindered by large variations in atomic structure, composition, and chemistry within nanometers or Ångstroms of the GB interface, which limits a fundamental understanding of electrical transport across and along GBs. Here we employ a novel correlated approach that is generally applicable to polycrystalline materials whose properties are affected by GB composition or chemistry. We demonstrate the connection between the nanoscopic chemical and transport properties of individual boundaries and the macroscopic ionic conductivity in oxygen-conducting $\text{Pr}_{0.04}\text{Gd}_{0.11}\text{Ce}_{0.85}\text{O}_{2-\delta}$. The key finding is that GBs with higher solute concentration have lower activation energy for cross-GB ion conduction through a polycrystalline conductor. The resultant semiempirical framework presented here provides a tool for understanding, designing and optimizing polycrystalline ionic conductors.



KEYWORDS: grain boundaries, ionic conductivity, electroceramics, correlated electron microscopy, precession electron diffraction, aberration-corrected scanning transmission electron microscopy, electron energy-loss spectroscopy

INTRODUCTION

Polycrystalline solids comprising grains connected at grain boundary (GB) interfaces with high point defect concentrations are ubiquitous throughout materials science and engineering. In bulk materials and thin films, grain boundaries directly influence mechanical, optical, thermal, magnetic, catalytic, and charge transport properties due to local heterogeneity in crystal structure, electronic structure, composition, and chemistry down to the atomic scale.^{1–9} For instance, Li^+ ion-conducting oxides used in solid-state batteries^{10–12} and O^{2-} ion-conducting solutions^{5,6,13–15} for solid oxide fuel/electrolysis cells and gas separation membranes fail to achieve maximum conductivity because ionic conductivity across GBs is often 2–6 orders of magnitude lower than that of conductivity through the grains.^{5,9,14,16–20}

Grain boundary effects can be magnified in polycrystalline thin films and nanoscale devices as the GB-effected regions can approach device sizes. Understanding the chemical and charge transport properties of grain boundaries in polycrystalline materials is important for developing ion-conducting solids for electrochemical energy conversion^{6,8,9,21} and storage^{10,22} but is challenging due to their complex, nanoscopic nature.^{5,8,9,21,23,24} Despite their wide-ranging scientific and technical relevance, optimizing GBs is complicated by diverse and significant

changes in atomic structure, composition, and chemistry within nanometers or angstroms of the boundary core relative to the adjacent grains.^{20,22,24–29} Furthermore, because of the rich diversity in GB types, there remains significant opportunity to establish a statistical link between nanoscale structure and macroscopic functionality. Thus, it is necessary to develop correlated approaches across varying length scales to provide a deeper understanding of ionic transport in polycrystalline materials.

In oxygen ion conductors, GB design strategies initially focused on mitigating the ionically blocking nature of glassy boundary-wetting phases formed by segregated impurity ions such as Si.^{17,30} However, low boundary conductivity persisted despite the use of high-purity chemical precursors and/or Si-scavenging solutes³¹ and is now widely understood as the depletion of positively charged oxygen vacancies in space-charge zones adjacent to boundary cores—where oxygen vacancies form preferentially and accumulate.^{32–34} (This space-charge formalism has also been applied to lithium-^{10,12} and proton-conducting^{35–37} polycrystalline oxides.) Within

Received: September 3, 2019

Accepted: December 4, 2019

Published: December 4, 2019

this context, there have been efforts to enhance cross-boundary oxygen conductivity by lowering the positive space charge potential of the boundary core through engineering of the local GB composition. For example, researchers showed that introducing transition metal cations to GBs, so-called heterogeneous doping, could alter the magnitude of the space-charge potential responsible for depletion of mobile oxygen vacancies.^{19,38,39} However, only a modest increase in GB conductivity was achieved, with the reported boundary conductivity still orders of magnitude lower than that of the grains. Moreover, the assumption of universal and uniform GB doping was not confirmed by using direct nanoscale GB chemical analyses. To our knowledge, there has been no experimental treatment of the statistical boundary-to-boundary correlation between character, composition, and ionic conductivity in a polycrystalline ion conductor. Thus, a better understanding of cross-boundary conductivity is still required to eliminate the deleterious influence of GBs on the overall ionic conductivity of many polycrystalline electrolytes. In a similar but orthogonal research area, recent studies of oxygen ion transport along GBs and dislocations in the perovskite Sr-doped LaMnO₃ have been shown to act as fast conduction pathways for oxygen ions,^{40,41} though prior simulations have indicated the opposite role of dislocations in Gd-doped ceria.⁴² Because perovskite oxides also exhibit tunable GB ionic conductivity, the experimental approach described here may thus be helpful in understanding mass transport along and across GBs. Such nuances in the properties of extended defects in electroceramics highlight the need to develop robust tools to elucidate interfacial structure–composition–conductivity relationships in these important materials.

It has been hypothesized that because there is a distribution in GB character within a polycrystalline material (i.e., the boundary atomic structure varies from GB to GB), there is a corresponding distribution in local GB composition, which yields a quantifiable distribution in the electrical conductivity of boundaries within a polycrystalline oxide.^{43–45} Previously, electrochemical measurements have been employed to measure the ionic conductivity of individual GBs,^{43–45} and the average conductivity of GB populations^{5,9,13,14,18} in polycrystalline electroceramics. A computational framework for understanding the statistical distribution of oxygen ion transport across grain boundaries in polycrystalline oxides has also been developed, for example.⁴⁶ High spatial resolution transmission electron microscopy (TEM) has provided nanoscopic elemental and chemical information from select boundaries,^{5,6,8,9,23,36,44,45,47} which was subsequently interpreted in terms of macroscopic charge transport. However, it has been difficult to establish a statistical connection between nanoscale structural and chemical measurements and macroscopic transport measurements of GBs in polycrystalline materials due to the complex diversity in local/nanoscale atomic structure, elemental composition, and chemistry. Too often studies that claim to focus on overall grain boundary conductivity are limited in scope and utility by investigating the properties of individual boundaries; thus, here we aim to combine quantitative characterization of multiple statistically distinct grain boundaries with a formalism that enables the prediction and, ideally, the optimization of macroscopic conductivity.

Recently, Ye et al. showed that for GBs in model bicrystals of Y_{0.08}Zr_{0.92}O_{1.96} (YSZ) the oxygen ionic conductivity across boundaries could vary by up to a factor of 10, which was

correlated to the relative misorientation of the two boundary-forming crystals (i.e., the GB character).⁴ This is a clear indication that the GB atomic structure in oxygen ion conductors is a tunable parameter for conductivity. Also in YSZ bicrystals, Feng et al. used atomic-resolution aberration-corrected STEM imaging and X-ray spectroscopy to show that local boundary composition varies with GB character.⁸ Together, these works clearly highlight the complex interplay between GB character, atomic-scale composition, and transport properties in model YSZ bicrystals. Noteworthy also is the use of microcontact impedance spectroscopy measurements across individual GBs in Fe-doped SrTiO₃ (predominantly an electron hole conductor) by Fleig et al.,⁴³ who demonstrated that a narrow distribution in the transport properties of boundaries was consistent with a conventional double-Schottky space charge model describing the distribution of point defects at GBs. However, no attempt to correlate these microcontact measurements with nanoscopic composition or GB character was reported, and as demonstrated below, the low solute concentration defect model used to describe the GBs in those materials is not applicable to the systems presented here. In related works on several Fe-doped SrTiO₃ low-angle bicrystal interfaces, De Souza et al. and Zhang et al. correlated electrical transport measurements and atomic structure with bicrystal misorientation angle and showed that GB blocking of p-type electronic carriers increased with misorientation angle for low-angle boundaries.^{44,45}

Here, we investigate the behavior of a polycrystalline oxygen ion conductor with high solute concentration (beyond the dilute solution limit) and solute-enriched GBs with local compositional heterogeneity. An analysis of the literature shows that the activation energy of GB conductivity is correlated to the grain boundary solute concentration. Thus, a detailed determination of variations in grain boundary solute concentration can be related to changes in grain boundary conductivity. This observation is the basis for the semi-empirical grain boundary conductivity model presented here. We employ a novel correlated electron microscopy approach to show a critical relationship between the relative misorientation of adjacent grains and the composition at GBs. This allows us to determine the GB conductivity distribution, which describes the boundary-to-boundary variation in ionic conductivity within a polycrystalline oxygen ion conductor. Furthermore, assuming oxygen ions diffuse via percolation through the most conductive GBs in a polycrystalline oxide, we hypothesize that only a subset of boundaries significantly contribute to net ionic conduction in polycrystalline electrolytes. Elucidating these GB properties, and developing novel methods for their characterization, will enable further design and engineering of optimized polycrystalline ceramics. Moreover, novel real-space maps of GB chemical and charge transport properties provide an exciting and informative visualization of these phenomena. When combined with suitable percolation models, the distribution can be employed to establish a direct link between nanoscopic materials property measurements and macroscopic ionic conductivity. These findings provide a statistical connection between experimentally derived GB character and composition distributions in polycrystalline materials (which consider boundary-to-boundary variations within a GB population) and the technologically relevant overall GB ionic conductivity. The approach should be applicable to other systems where a

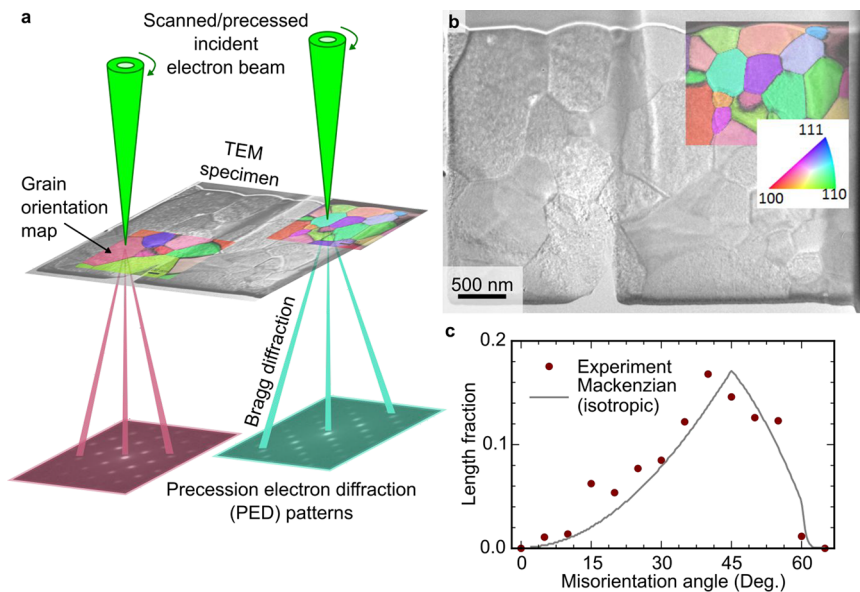


Figure 1. Grain boundary character was determined by using nanobeam transmission electron diffraction. (a) Grain orientation mapping via nanobeam precession electron diffraction. (b) Bright-field TEM image of PGCO specimen with a representative grain orientation map overlaid; grain orientation is indicated by the inset color-coded stereographic section. (c) Misorientation angle distribution (MAD) derived from measured grain orientation data (Experiment) and analytical MAD for the randomly oriented cubic system (Mackenzian (isotropic)).

correlation exists between GB solute concentration and activation energy of ion conduction.

We combine grain orientation imaging and targeted nanoscale spectroscopy of GBs to characterize, and report for the first time, a so-called GB conductivity distribution in the polycrystalline oxygen ion conductor $\text{Pr}_{0.04}\text{Gd}_{0.11}\text{Ce}_{0.85}\text{O}_{2-\delta}$ (PGCO)—a fluorite oxide predicted theoretically^{48,49} and shown experimentally⁵ to have higher anionic conductivity than $\text{Gd}_x\text{Ce}_{1-x}\text{O}_{2-\delta}$. The conductivity distribution is a direct byproduct of nonuniformity in solute segregation behavior to GBs and is a tunable parameter for optimizing conductivity of polycrystalline materials. We demonstrate that as the GB misorientation angle increases, most boundaries exhibit greater solute segregation, which lowers the activation energy of GB ionic conduction, yielding GBs with higher oxygen ionic conductivity. We show that local GB composition varies mostly with character, making it possible to predict the ionic conductivity of individual boundaries from knowledge of their character, which can be determined experimentally relatively quickly for hundreds or thousands of boundaries. Local composition data are interpreted quantitatively to predict the chemical and transport properties of GBs. The distribution in boundary conductivity is estimated for an entire GB population enabling explicit identification of boundaries participating in oxygen ion percolation through the material. By incorporating the influence of GB composition on measured and simulated properties, we demonstrate a greatly improved understanding of the nature of boundaries and a powerful new framework for predicting GB properties. Furthermore, unique real-space maps of chemical and charge transport properties of boundaries are presented, making this work relevant to polycrystalline materials with properties influenced by GBs. Novel insights presented here will facilitate the design of GBs with optimized chemical and transport properties, which remains a considerable materials challenge.

RESULTS AND DISCUSSION

Measuring Grain Boundary Character. To determine the oxide's GB character, grain orientation mapping using a spatially resolved transmission electron diffraction technique was used to measure the GB misorientation angle distribution (MAD), which indicates the fractional length of boundaries with a given misorientation angle between adjacent grains. This nanobeam TEM technique employs precession electron diffraction (PED) to quantify grain orientation by automated acquisition and indexing of transmission electron diffraction data sets^{50,51} (Figure 1a and Methods section). This method quantifies grain orientation but does not resolve the GB plane. A representative grain orientation map is overlaid on a bright-field TEM image of the polycrystalline specimen in Figure 1b. Each grain is colored per the inset stereographic section, which indicates the crystallographic direction oriented parallel to the incident electron beam direction. The measured MAD (Figure 1c) agrees reasonably well with the analytical solution for a material with cubic crystal symmetry and randomly oriented (isotropic) grains⁵² as well as with MADs measured in other fluorite oxides such as zirconia⁵³ and ceria-based⁹ ion conductors, confirming that the present material exhibits a random distribution of grain orientations. This analysis also shows that coincident-site-lattice-type GBs—oft-investigated model boundaries—comprise only ~23% of the total boundary length (Figure S2), highlighting the importance of sampling a range of different boundary types in polycrystalline oxides.

Measuring Grain Boundary Composition. Based on the grain boundary character analysis, a sample of 12 GBs spanning the range of misorientation angles in the MAD (Figure 1c) was selected for detailed chemical nanoanalysis by aberration-corrected (AC) STEM core-loss EELS (Methods section). Representative AC-STEM annular dark-field (ADF) images are presented in Figure 2a,b, wherein bright spots indicate the positions of cation columns. Figure 2c–f compares energy-loss spectra acquired in the grains several nanometers from GB cores and spectra acquired at the boundary cores

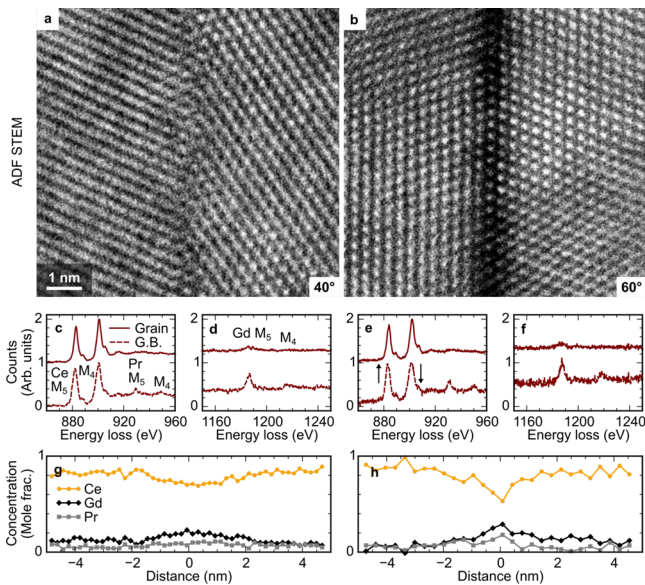


Figure 2. Grain boundary cation composition was measured using electron energy-loss spectroscopy in an aberration-corrected scanning transmission microscope. (a, b) Atomic-resolution aberration-corrected STEM (AC-STEM) annular dark field images of grain boundaries (GBs) with misorientation angles of 40° and 60° , respectively. (c–f) Electron energy-loss spectra acquired in grains, i.e., >5 nm, from the GB core (Grain), and at the GB cores (G.B.) shown in (a) and (b), respectively; Ce and Pr M₄₅ edges are shown in (c, e) and Gd M₄₅ edges (multiplied by two for easier comparison) in (d, f). (g, h) Cation concentration profiles derived from EELS line scans across the GBs in (a) and (b), respectively; the GB core is located at 0 nm. The estimated fractional error in the absolute cation concentrations is $\leq 15\%$ (see Methods section).

shown in Figure 2a,b. The Ce (~ 883 eV), Pr (~ 905 eV), and Gd (~ 1185 eV) M₄₅ EELS edges were used to quantify the spatial distribution of the three cations at GBs (Methods section), and cation concentration profiles are presented in Figure 2g,h corresponding to the energy-loss spectra in Figure 2c–f. The profiles show that a decrease in the Ce concentration is accompanied by a corresponding increase in both Pr and Gd concentrations, indicative of the nanoscale accumulation of Pr and Gd solute cations in the GB vicinity. The mean width of the concentration profiles was determined to be 2.1 ± 0.6 nm at half-maximum, consistent with previous experimental^{2,5,9,26,29} and theoretical^{21,26} studies of ceria solid solutions. In this case, solute segregation to boundaries occurs during high-temperature sintering at 1350 °C (Methods section) and is likely driven by elastic effects associated with ionic radius mismatch between solute and host cations, Coulombic attraction between the positive GB core and the solute point defects which carry negative charge relative to the host cation (e.g., Gd³⁺ and Pr³⁺ substituting for Ce⁴⁺, or Gd'_{Ce} in Kröger–Vink notation), and minimization of boundary energy.⁷ Whereas Gd is a trivalent solute (106 pm radius when 8-fold coordinated),⁵⁴ Pr is a multivalent substitutional cation and is expected to be in the 4+ (113 pm) and/or 3+ (96 pm) oxidation states depending on temperature. In Pr_{0.1}Ce_{0.9}O_{2- δ} , Bishop et al. showed that during heating Pr⁴⁺ is reduced to Pr³⁺ above ~ 850 °C and an oxygen partial pressure of 0.21 atm.¹⁵ Thus, during sintering at 1350 °C here, Pr is likely Pr³⁺. In some cases, the relative peak intensity of the Ce M₄ and M₅ peaks was also found to change at GBs (e.g., peaks indicated in

Figure 2e with arrows) indicative of a Ce valence change from +4 to +3, likely the result of oxygen vacancies formed to accommodate structural incoherence of the boundary core, or the indication of the GB space charge which need not be charge neutral.^{2,5} There was significant variation in the degree of solute enrichment at GBs, which illustrates the need to measure a representative and diverse sampling of boundaries to more accurately characterize a polycrystalline material.

Grain Boundary Composition Distribution. All GBs are solute-enriched and Ce-deficient, with the boundary solute concentration trend increasing with misorientation angle (Figure 3a). Cation concentrations were determined from the maxima/minima (at 0 nm) of concentration profiles (e.g., Figure 2g,h). As expected, the grain cation concentrations are scattered about the nominal values (Table 1). Solute segregation to boundaries can minimize the overall system energy by lowering the GB energy,^{2,55} and there is experimental evidence indicating that the boundary energy in metal oxides tends to increase with misorientation angle,⁵⁶ suggesting that the observed solute segregation trend is in part associated with lowering of GB energy. Hence, misorientation angle appears to represent a tunable parameter that can influence GB properties in polycrystalline materials via modification of local composition. To demonstrate the construction of semiempirical framework, we assume a linear dependence of solute concentration on misorientation angle, though the actual solute composition may exhibit a nonlinear dependence on misorientation angle—as does GB energy.⁵⁶ Indeed, a single parameter descriptor GB character may in fact be insufficient because GBs with similar misorientation angles can have different atomic structure at the GB plane and thus energy driving solute segregation. Future improvement of this framework should likely focus on increasing the number of sampled misorientation angles and integration of multi-parameter descriptors of the GB plane. In spite of these limitations, we show that the single parameter descriptor assumption provides considerable insight into the overall behaviors of the ionic conductivity and gives a robust nanoscale statistical model which yields predictions that are in agreement with macroscopic impedance spectroscopy.

Figure 3a and Table 1 indicate that Gd³⁺ segregation is more pronounced to high-angle GBs than Pr³⁺. We do not currently have a compelling explanation for this behavior. Higher-angle GBs are generally thought to have more free volume and higher energy, providing a larger global driving force for solute segregation. However, from an atomistic perspective it is hard to say with specificity to which GB core sites or core-adjacent lattice sites the segregating dopants are diffusing or to identify the local driving force. Aidhy et al. recently used atomistic simulations of lanthanide dopant segregation to a series of coincident-site lattice type symmetric tilt interfaces in ceria to show that dopant segregation tendency decreased as the dopant cation radius approached that of the host.^{57,58} However, they recognized the limited scope of their work and encouraged further systematic experimental studies of dopant segregation.

The misorientation-dependent GB solute concentration was fit with a straight line (Figure 3a; Table 1 for parameters) and then combined with the Mackenzian distribution, allowing the solute concentration at all boundaries in the sample to be estimated. This analysis allows us to statistically connect a small but detailed set of nanoscale composition measurements to the entire population of GBs in the polycrystalline oxide.

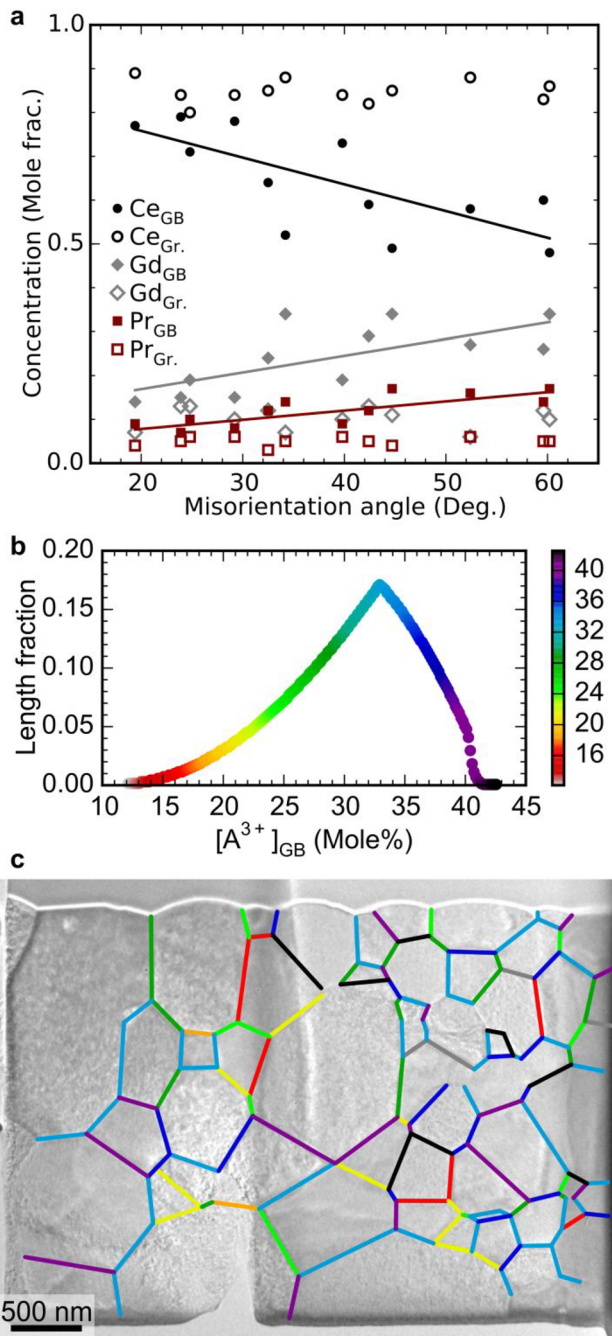


Figure 3. Grain boundary solute concentration was measured as a function of grain boundary misorientation angle and correlated to grain boundary character. (a) Dependence of grain (Grain) and grain boundary (GB) cation concentration on misorientation angle. Linear fits to the data are indicated for each cation (coefficients in Table 1). (b) Length fraction distribution of the effective trivalent solute concentration, $[A^{3+}]_{GB}$, measured at GBs; the scale bar corresponds to the data marker colors and $[A^{3+}]_{GB}$. (c) Bright-field TEM image of PGCO specimen with GB segments colored to indicate their effective trivalent solute concentration, $[A^{3+}]_{GB}$, in accordance with the scale bar in (b).

(This novel correlated approach to characterize GB composition is quantitatively superior to analysis based on randomly sampled GBs (Figure S3)). Figure 3b presents the resultant length fraction distribution of the so-called effective GB trivalent solute concentration, $[A^{3+}]_{GB}$, where $[A^{3+}]_{GB} =$

Table 1. Grain and GB Cation Concentrations Assuming Normal Distribution and Linear Coefficients Describing the Dependence of Boundary Cation Concentration on Misorientation Angle per $[Cation]_{GB} = A \cdot (\text{Misorientation Angle}) + B$

	Ce	Gd	Pr
nominal conc (mol fraction)	0.85	0.11	0.04
grain conc (mol fraction)	0.85 ± 0.03	0.10 ± 0.03	0.05 ± 0.01
grain boundary conc (mol fraction)	0.62 ± 0.10	0.26 ± 0.07	0.13 ± 0.03
linear coeff $A \times 10^{-3}$ (mol fraction/deg)	-6.1	3.8	2.1
linear coeff $B \times 10^{-2}$ (mol fraction)	88	9.3	3.6

$[Gd^{3+}]_{GB} + [Pr^{3+}]_{GB}$ (Figure S4). These data enable identification of the average $[A^{3+}]_{GB}$ of each GB segment in the specimen from knowledge of its misorientation angle (Figure 3c). The single descriptor approximation linking grain boundary composition and angle allows us to generalize high-spatial-resolution composition data to an entire population of boundaries in polycrystalline materials.

Grain Boundary Conductivity Distribution. To determine the GB ionic conductivity distribution from the boundary solute concentration distribution (Figure 3b), we first identified a relationship between GB solute concentration, $[A^{3+}]_{GB}$, and activation energy of GB ionic conductivity, E^{GB} , which governs ionic conductivity, σ_{GB} via eq 1. Here, β_{GB} is the carrier-concentration-independent conductivity pre-exponential, n_v^{GB} the effective GB carrier concentration (i.e., the oxygen vacancy concentration, omitting spatial variations), T the temperature, and k the Boltzmann constant.⁹

$$\sigma_{GB} = \beta_{GB} \frac{n_v^{GB}}{T} \exp\left(\frac{-E^{GB}}{kT}\right) \quad (1)$$

An empirical relationship between E^{GB} and $[A^{3+}]_{GB}$ was derived from published values of E^{GB} measured in $Gd_xCe_{1-x}O_{2-\delta}$ (Figure 4a). Although the EELS measurements of $[A^{3+}]_{GB}$ presented above were derived from a PGCO specimen, a literature survey yielded no relevant correlated data on this system. Thus, we utilized instead published data on $Gd_xCe_{1-x}O_{2-\delta}$ to develop the present framework. The valence of Pr was not determined here because of the difficulty in experimentally quantifying the shift of the Pr M₄₅ white lines to lower energy loss values when Pr changes valence. Details of this quantification process are available in our previous work.⁵⁹ As discussed above and in Figure S4, Pr is a minor solute in this case so the exact concentration of trivalent Pr does not strongly influence our demonstration of the new framework.

Of the $[A^{3+}]_{GB}$ values plotted in Figure 4a, only one data point is from a publication that reported both E^{GB} and GB solute concentration measured in the same material (red triangle in Figure 4a at mole fraction of 0.6).⁵ The rest of the $[A^{3+}]_{GB}$ data points were estimated from studies that reported nominal solute concentration and E^{GB} using eq S1 (see Figure S5 for details). The “decaying exponential” fit (black curve in Figure 4a), described by the inverse power law of eq 2, is the best fit of these data which passes through the red triangle (which we give stronger weighting to because it is based on a direct measurement of E^{GB} and $[A^{3+}]_{GB}$).

$$E^{GB} = 2 \times 10^{-4} ([A^{3+}]_{GB})^{-5} + 0.91 \quad (2)$$

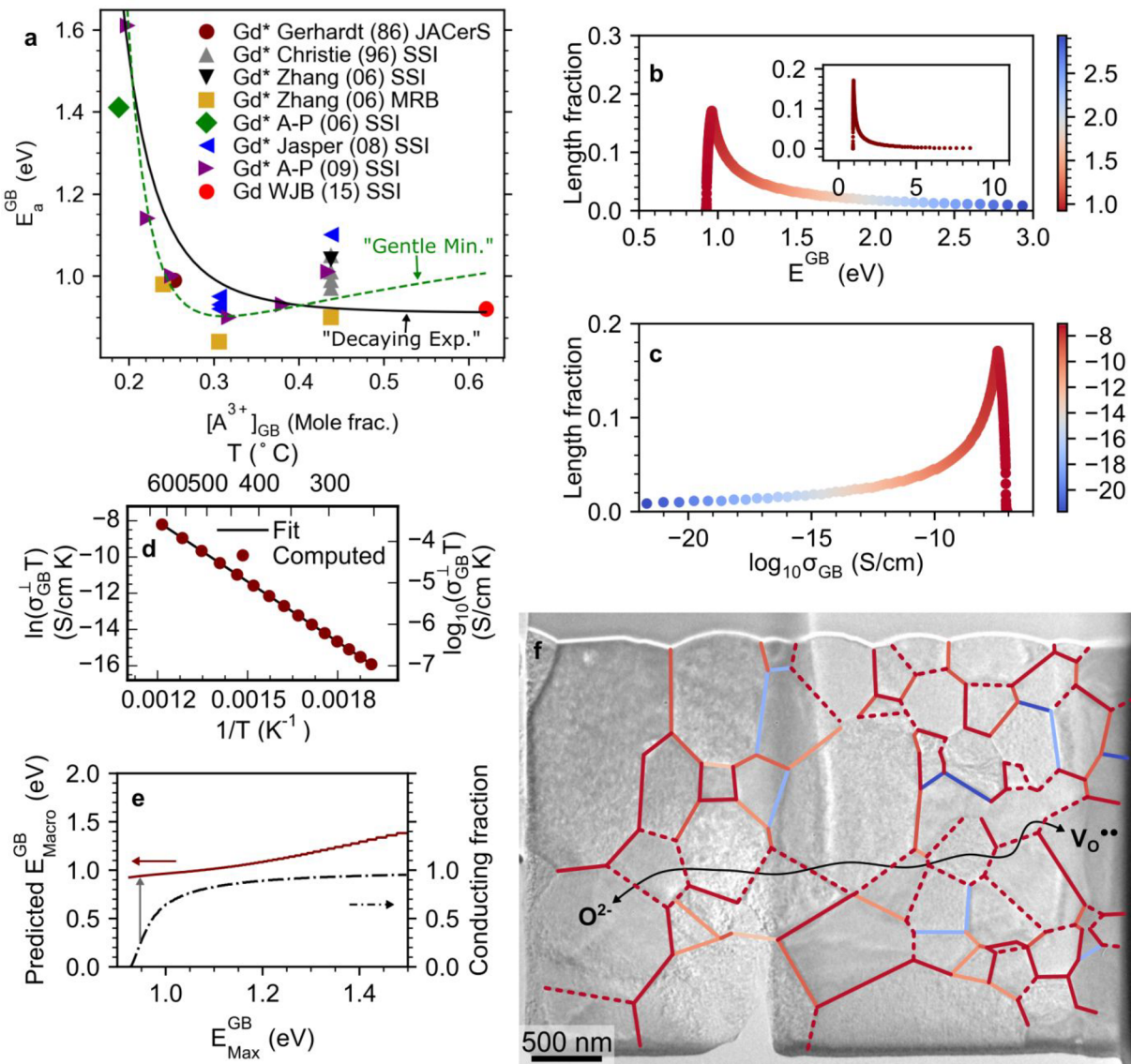


Figure 4. Grain boundary transport properties were modeled for all grain boundaries and mapped in real space. (a) Literature data showing the relationship between the activation energy of grain boundary conductivity (E_{gb}^{GB}) and $[A^{3+}]_{gb}$ for comparable $\text{Gd}_x\text{Ce}_{1-x}\text{O}_{2-\delta}$ solid solutions; the legend indicates if the data were measured directly or inferred using eq S1 (labeled with * if inferred; see Figure S5).^{5,14,19,20,60–62} The data are fit via eq 2, the so-called “exponential decay” fit (black solid curve), and the “gentle minimum” fit (green dashed curve). (b) Distribution of E_{gb}^{GB} for the experimental sample PGCO, with expanded view inset. (c) GB conductivity distribution calculated using eq 1 for $T = 440^\circ\text{C}$. (d) Effective GB conductivity along percolating path computed via eq 3, with $E_{Max}^{gb} = 0.97$ eV. (e) Predicted E_{Macro}^{gb} and conducting GB fraction as a function of E_{Max}^{gb} (eq 3). (f) Bright-field TEM image with GB segments colored to indicate E_{Macro}^{gb} and conductivity per the scale bars in (b) and (c). Boundary segments are indicated with dashed lines to indicate GBs participating in ion/vacancy percolation, and the double-headed arrow indicates a potential percolating path for ions/vacancies. Reproduced in part with permission from ref 5. Copyright 2015 Elsevier B.V. Reproduced in part with permission from ref 14. Copyright 2009 The Royal Society of Chemistry. Reproduced in part with permission from ref 19. Copyright 2006 Elsevier B.V. Reproduced in part with permission from ref 20. Copyright 2008 Elsevier B.V. Reproduced in part with permission from ref 60. Copyright 1986 John Wiley and Sons. Reproduced in part with permission from ref 61. Copyright 1996 Elsevier B.V. Reproduced in part with permission from ref 62. Copyright 2006 Elsevier Ltd.

There is considerable scatter in the data, and it is also possible to fit a function with a gentle minimum to the data (green curve in Figure 4a; see also Figure S6). However, the change in functional form makes only a very small change in the E_{gb}^{GB} distribution and the conductivity distribution (discussed below). As discussed below, the change in the derived effective E_{Macro}^{gb} is from 0.94 eV by using the black “decaying exponential” fit to 0.92 eV using the “gentle minimum” fit. The reason that the change in functional form has little effect on the ionic conductivity is because the largest difference

between the gentle minimum and decaying exponential fits occurs only for GB solute concentration greater than 0.5. Such high GB solute concentrations are not present in the materials employed here (see Figure 3b and Figure S4).

Figure 4a indicates that E_{gb}^{GB} initially decreases strongly as $[A^{3+}]_{gb}$ increases up to ~ 0.3 and thereafter continues to change more slowly with increasing GB solute content. This suggests that according to eq 1, increasing $[A^{3+}]_{gb}$ should increase σ_{gb} via concomitant decrease in E_{gb}^{GB} , which has been verified empirically by Shirpour et al. for proton conduc-

tors^{36,47} and by Bowman et al. for the oxygen conductor $\text{Ca}_x\text{Ce}_{1-x}\text{O}_{2-\delta}$.⁹ The decrease in E^{GB} with increasing local GB solute concentration was explained theoretically by Shirpour et al.,³⁶ who claimed that annealing their Sc- and Y-substituted BaZrO_3 samples caused the GBs to transform from Mott–Schottky type GBs (constant solute concentration across the boundary with concentration profile defined by dilute-solution thermodynamics, eq S6) to Gouy–Chapman type GBs (variable solute concentration across the boundary with concentration profile defined by dilute-solution thermodynamics, eq S6), which reduced the GB carrier depletion widths sufficiently to increase conductivity. Similarly, the decrease in E^{GB} with nominal solute concentration was linked to a decrease in the GB space charge potential by Avila-Paredes et al. (the local GB solute concentration was not measured in that work), again using a Mott–Schottky dilute-solution space-charge model.¹⁴ It is important to point out that the high GB solute concentrations measured here and reported previously^{3,5,9,21,26,63,64} suggest that models which assume either constant or dilute-solution concentration profiles across the GB are not valid for many ceria-based electrolytes.

To illustrate the problems associated with applying conventional dilute-solution space-charge theory to the high solute concentration boundaries presented here, we applied the Gouy–Chapman model to our experimental solute profiles (Figure S7). These simulations suggest that the boundary conductivity should decrease with increasing GB solute concentration (via increased space charge potential), contradicting the published data in Figure 4a which indicate that GB conductivity increases with increasing GB solute concentration via reduced E^{GB} . We believe these contradictions are a consequence of the high GB solute concentration and assert that further theoretical development is required to elucidate the origin of decreasing E^{GB} with increasing GB solute segregation.

The distribution of activation energy of GB conduction (or E^{GB} distribution) for the sample discussed here is determined by applying eq 2 to the GB solute concentration distribution (Figure 3b), yielding Figure 4b. This distribution indicates the length fraction of GBs with various values of E^{GB} and shows that for a plurality of GBs $E^{\text{GB}} \approx 1.0$, with 65% of GBs exhibiting $0.93 \text{ eV} < E^{\text{GB}} \leq 1.05 \text{ eV}$ and 35% of boundaries exhibiting higher activation energies. Inserting the E^{GB} distribution into eq 1 produces the GB ionic conductivity distribution (σ_{GB} distribution) shown in Figure 4c, which indicates the length fraction of GBs with given values of σ_{GB} and shows that for most boundaries $10^{-9} \text{ S/cm} < \sigma_{\text{GB}} < 10^{-7} \text{ S/cm}$ at 440°C . Here, n_v^{GB} was approximated as $[\text{A}^{3+}]_{\text{GB}}/2$ based on recent theoretical work indicating that oxygen vacancies mostly coaccumulate at GBs with trivalent solutes in concentrated gadolinia–ceria solid solutions that have high solute concentration near GBs.^{21,65} β_{GB} was taken to be 10^3 so that the conductivity of the most conducting GBs in the σ_{GB} distribution was $\sim 10^{-7} \text{ S/cm}$ at 440°C , consistent with typically reported values.^{5,9,14,17,19,20,31,61,62} (As the compiled data from the literature exhibit considerable scatter, we varied the coefficients of eq 2 and recalculated the E^{GB} and σ_{GB} distributions to ensure they are qualitatively robust against fitting errors originating from data scatter (Figure S6).)

While the activation energy of GB ion conduction term dominates the behavior of eq 1, rigorous treatments of both n_v^{GB} and the pre-exponential factor, β_{GB} , are certainly warranted (with the latter possibly accessible using experimental methods

like AC impedance spectroscopy), as these quantities should exhibit a more complex dependence on $[\text{A}^{3+}]_{\text{GB}}$ and temperature.²¹ Nevertheless, to the best of our knowledge, this is the first reported estimate of E^{GB} and σ_{GB} distributions in an entire GB population determined from direct experimental measurements of boundaries in a polycrystalline material. In future iterations of the proposed framework, it will be advantageous to perform a more comprehensive empirical determination of the relationship between GB composition and E^{GB} .

Linking Nanoscale and Macroscale Ionic Transport Properties.

To rationalize the transport property distributions above, and to validate our methodology, we constructed a model to directly link nanoscopic conductivity of individual boundaries with macroscopic conductivity, measured, for instance, by using impedance spectroscopy. We assumed that ions/vacancies migrate through a polycrystalline material via three-dimensional bond percolation, where GBs are paths between grains that are open or closed depending primarily on the activation energy of grain boundary conductivity, E^{GB} . Within this framework, a conducting path connecting two points in the material (i.e., through the polycrystalline electrolyte) will exist if the probability of a bond being open exceeds some critical probability, the so-called percolation threshold,⁶⁶ γ . For a polycrystalline solid like that investigated here, whose grain shapes can be approximated as a Kelvin tetrakaidecahedron (eight hexagonal facets and six square facets), the percolation threshold was found to be 0.23 by using Monte Carlo simulations.⁶⁶

We assume that only GBs with $E^{\text{GB}} < E_{\text{Max}}^{\text{GB}}$ are open, and therefore an experimental macroscopic conductivity measurement will probe ion/vacancy motion through these GBs. As derived in eqs S9–S23, the macroscopic GB conductivity of a percolating path, $\sigma_{\text{GB}}^{\perp}$, can be related to the properties of individual grain boundaries along the path through eq 3.

$$T\sigma_{\text{GB}}^{\perp} = \frac{\beta_{\text{GB}}\gamma}{\sum_{j=1}^N \frac{d_j}{n_j^{\text{GB}}} \exp\left(\frac{E_j^{\text{GB}}}{kT}\right)} \quad (3)$$

As in eq 1, β_{GB} is the carrier-concentration-independent conductivity pre-exponential. The percolation threshold, γ (eq S22), may be known for a given microstructure or deduced by using this model based on knowledge of a material's macroscopic activation energy of GB conduction. d_j is the material's overall probability distribution of GBs—each of distinct type j (with carrier concentration, n_j^{GB} , and conduction activation energy, E_j^{GB}). The GB probability distribution (Figure 1c), carrier concentrations (via Figure 3a), and conduction activation energies (Figure 4a) were determined from the TEM measurements reported here and published data. The summation in the denominator (up to $j = N$) is from the lowest activation energy GBs up to some cutoff maximum value $E_{\text{Max}}^{\text{GB}}$ such that a complete percolating conducting path arises. Using eq 3 to plot $\ln(T\sigma_{\text{GB}}^{\perp})$ vs $1/T$ for typical values of the parameters yields a straight line, as shown in Figure 4d. This is essentially an Arrhenius plot, and the activation energy derived from the gradient of this graph, $E_{\text{Macro}}^{\text{GB}}$, is an effective activation energy of GB ionic conduction determined in a macroscopic measurement of GB ionic conductivity such as impedance spectroscopy.

From a fit of $\ln(T\sigma_{\text{GB}}^{\perp})$ vs $1/T$, it is possible to predict $E_{\text{Macro}}^{\text{GB}}$ and the conducting GB fraction as a function of the cutoff, $E_{\text{Max}}^{\text{GB}}$ (Figure 4e). The conducting GB fraction depends strongly on

$E_{\text{Max}}^{\text{GB}}$ below ~ 1.05 eV, reflecting the greater prevalence of GBs in that range of E^{GB} values (Figure 4b), and asymptotically approaches unity for greater values of $E_{\text{Max}}^{\text{GB}}$. Figure 4e shows that the predicted macroscopic activation energy of GB conduction ranges from 0.93 to 1.4 eV depending on the fraction of GBs involved in transport.

The model was validated by first using the percolation threshold of $\gamma = 0.23$ ⁶⁶ to determine the value of N in eq S22, then by using eq 3 and the Arrhenius relationship to predict $E_{\text{Macro}}^{\text{GB}}$, and finally comparing this to reported activation energies of conduction measured by impedance spectroscopy. For the current experiment, the GB composition distribution was determined for a sample with nominal trivalent solute concentration, $[A^{3+}]$, of 0.13. For typical $\text{Gd}_x\text{Ce}_{1-x}\text{O}_{2-\delta}$ samples with this $[A^{3+}]$ subject to similar heat treatments, one can expect the corresponding $[A^{3+}]_{\text{GB}}$ to be about 0.35 (Figure S5), which should yield activation energies of GB conduction around 0.95 eV according to the published data in Figure 4a. In Figure 4e, setting the percolation threshold to 0.23 (i.e., the conducting fraction of GB) gives $E_{\text{Max}}^{\text{GB}}$ of 0.97 eV, which yields a predicted $E_{\text{Macro}}^{\text{GB}}$ of 0.94 eV, in good agreement with published literature.¹⁴ Again, the effective $E_{\text{Macro}}^{\text{GB}}$ derived by using the black “decaying exponential” fit changes from 0.94 to 0.92 eV if derived via the “gentle minimum” fit.

A further check of the model is its ability to predict the change in GB conductivity with changes in average GB composition. A detailed set of measurements of grain boundary character, composition, and conductivity were published for a series of $\text{Ca}_x\text{Ce}_{1-x}\text{O}_{2-\delta}$ samples.⁹ That work showed that changing the average GB Ca^{2+} concentration from 18 to 40 mol % produced an increase in boundary ionic conductivity by nearly 4 orders of magnitude, with the E^{GB} dropping from 1.5 to 1.0 eV. Here, we conducted a simulation of a similar change in the GB composition using the concentration distribution model (Figure S8). In this simulation, the material’s MAD (Mackenzian in Figure 1c) was scaled so that the length fraction distribution peaked at $[A^{3+}]_{\text{GB}}$ of ~ 20 mol % (Figure S8b). This resulted in the model predicting a drop in GB ionic conductivity by nearly 4 orders of magnitude (e.g., from 2.5×10^{-8} to 3.6×10^{-12} S/cm at 410 °C), with $E_{\text{Macro}}^{\text{GB}}$ increasing to 1.48 eV (from 0.95 eV), in very good agreement with the published data.⁹

Having validated our multimodal correlated approach, we finish by giving a visual representation of the model by showing a real space map of the individual conductivities of a collection of boundaries in a polycrystalline ceramic (Figure 4f). In this map, the boundary segments are colored according to their individual E^{GB} and σ_{GB} values by using the scale bars in Figure 4b,c. Segments indicated with dashed lines represent boundaries which participate in ion/vacancy percolation, and the double-headed arrow indicates a potential transport path for ions/vacancies. This model provides a powerful statistical approach for linking the nanoscopic distributions of GB composition with macroscopic measurements of GB composition. Additionally, it provides a tool to explore how variations in microstructure arising from differences in materials processing will control macroscopic functionality.

The overall utility of the model presented here is that it can easily be adapted to polycrystalline samples with different microstructures. For random grain boundary microstructures where there is a simple relationship between orientation and grain boundary composition, the percolation threshold of 0.23 should be applicable for cases where there are many grains

along the conducting path. Essentially this means the grain size is much smaller than the conducting path length. As the conducting path length becomes shorter (or the grain size becomes larger), for the same material it will be necessary to include pathways with higher activation energy of GB conduction to create a conducting path. However, more extensive annealing of the sample may drive more solute to the GB resulting in a reduction in the activation energy of GB conduction. For textured thin films grown at low temperature, grain boundary segregation is small so it may be beneficial to anneal such films for extended periods of time to drive solutes to the grain boundaries. The grain boundary distribution will not follow the MacKenzie distribution, but it should be feasible to directly determine the grain boundary composition distribution by using STEM EELS or energy-filtered imaging.

CONCLUSION

A novel semiempirical framework was demonstrated that enabled determination of the grain boundary conductivity distribution—a description of the boundary-to-boundary variability in ionic conductivity in the GB population of a polycrystalline ion conductor. The key finding is that GBs with higher solute concentration have lower activation energy of cross-GB ion conduction through a polycrystalline material. A correlated experimental approach combining precession electron diffraction orientation imaging and electron energy-loss spectroscopy was used to extend nanoscale grain boundary composition measurements to an entire grain boundary population in an oxygen conducting electrolyte. This statistical approach, when combined with published activation energies of GB conduction, produces real-space maps of GB chemical and transport properties and provides a tool for developing polycrystalline electrolytes with tailored GB conductivities. Explicitly, we show that in oxygen-conducting $\text{Pr}_{0.04}\text{Gd}_{0.11}\text{Ce}_{0.85}\text{O}_{2-\delta}$ GBs with greater misorientation angle exhibit higher solute concentration, which empirically lowers their activation energy of cross-GB ion conduction. By explicitly correlating physical and transport properties across length scales, we demonstrate the potential for bottom-up design and optimization via control of the statistical distribution of GB character and/or composition. The ability to generalize high-spatial-resolution observations to an entire boundary population in a polycrystalline material is a step forward in characterizing polycrystalline materials. We visualize the relative conductivity of individual GBs in a TEM specimen and generate a map of the subset of boundaries comprising the percolating ionic conduction pathway in the polycrystalline material. This provides a new approach for linking nanostructure and macroscopic functionality and contributes to understanding the nature of ionic conductivity associated with GBs in polycrystalline ceramic materials.

METHODS

Material Synthesis and Pellet Fabrication. $\text{Pr}_{0.04}\text{Gd}_{0.11}\text{Ce}_{0.85}\text{O}_{2-\delta}$ nanoparticles were synthesized by the authors from hydrated nitrate salts (99.999% purity, Alpha Aesar) by using spray drying.⁵ Synthesized powder was compacted to a pellet that was sintered in air at 1350 °C for 18 h to produce a dense polycrystalline material with grain size of 450 ± 180 nm, detailed in ref 5. Considering high-resolution bright-field TEM observations (e.g., Figure S1) and the high-purity precursors employed here, the presence of amorphous intergranular phases was assumed negligible.

TEM Specimen Preparation. An electron-transparent specimen was prepared for TEM measurements from the PGCO pellet via

standard lift-out techniques using a scanning electron microscope equipped with a Ga⁺ focused ion beam column (Nova 200 NanoLab, FEI). Thinning the specimen was performed by using Ga⁺ ions with energy ranging from 30 to 2 kV.⁵

Precession Electron Diffraction (PED). Grain orientation data were acquired by using a 200 kV JEOL ARM 200F S/TEM equipped with an ASTAR PED system (NanoMegas, USA). Serial diffraction patterns were acquired automatically with 5 nm step intervals, and diffraction patterns were indexed to fluorite CeO₂ (*Fm*3*m*) by using the TopSpin software (AppFive LLC, USA). PED data were exported from TopSpin as Euler angles and read into the EDAX TSL OIMS software to generate MAD and CSL distributions. No correlation relating the orientation of adjacent grains was assumed.

Electron Energy-Loss Spectroscopy (EELS). The aforementioned STEM was also equipped with a spherical aberration corrector (AC) and Gatan Enfina energy-loss spectrometer. Spatially resolved AC-STEM EELS data were acquired via one-dimensional line scans perpendicular to the GBs. Three or four measurements were performed at each GB, from which the mean and standard deviation in the cation concentration of the GB core could be determined. Only GBs deemed to be parallel to the electron optic axis were analyzed. The EELS convergence and collection semiangles were 20 and 42 mrad, respectively.

Spectra were calibrated by setting the Ce M₅ edge maximum to 883 eV; an inverse power law function was used to model the pre-edge background intensity for background extrapolation and subtraction.^{67,68} A two-window background interpolation fitting procedure was applied to the Pr M₄₅ edge to account for edge overlap effects. Background fitting and signal integration windows were selected to minimize extrapolation errors and artifacts such as plural scattering (Table S1). Ion concentrations were estimated via eq 4, where C_A and C_B are concentrations of elements A and B. I_A and I_B are integrated EELS signal intensities, and σ_A and σ_B are the electron scattering cross sections. The cross-section ratios, so-called *k*-factors, were determined from average values measured in grains, where the nominal composition was assumed (Table S1). Care was taken to minimize uncertainty in the *k*-factor determination, though a systematic error of ≤15% in the absolute elemental concentration can be expected by using this method.^{67,68}

$$\frac{C_A}{C_B} = \frac{I_A \sigma_B}{I_B \sigma_A} = \frac{I_A}{I_B} k_{AB} \quad (4)$$

Data Processing. Micrographs and EELS data were processed by using the Gatan DigitalMicrograph software suite and the Python Pyzo integrated development environment (open source). Figures were prepared by using the Inkscape graphics editor (open source).

ASSOCIATED CONTENT

Supporting Information

The Supporting Information is available free of charge at <https://pubs.acs.org/doi/10.1021/acsmami.9b15933>.

Coincident site lattice type boundaries; comparing correlated approach with random GB sampling; effective grain boundary trivalent solute concentration; relating activation energy of GB conduction and solute concentration; predicting solute segregation using the Gouy–Chapman model; derivation of model for grain boundary conductivity distribution; demonstrating the predictive capability of the model; supplemental references (PDF)

AUTHOR INFORMATION

Corresponding Authors

*E-mail: crozier@asu.edu.

*E-mail: will.bowman@uci.edu.

ORCID

William J. Bowman: 0000-0002-4346-1144

Peter A. Crozier: 0000-0002-1837-2481

Present Address

W.J.B.: Department of Materials Science and Engineering, University of California, Irvine.

Author Contributions

W.J.B. and P.A.C. designed the study. A.D. performed the PED data acquisition. W.J.B. performed all other experiments, all data processing, modeling, and generation of figures. W.J.B. and P.A.C. analyzed the data. P.A.C. supervised the work.

Notes

The authors declare the following competing financial interest(s): A.D.D. is an employee of AppFive LLC, which commercializes the TopSpin software used in this work. No other competing financial interests are declared.

ACKNOWLEDGMENTS

W.J.B. acknowledges the National Science Foundation's Graduate Research Fellowship (DGE-1211230) for financial support. W.J.B. and P.A.C. acknowledge support of NSF Grant DMR-1308085. We gratefully acknowledge access to the John M. Cowley Center for High Resolution Electron Microscopy and the Southwestern Center for Aberration-Corrected Electron Microscopy at Arizona State University.

DEDICATION

Dedicated to Lily.

REFERENCES

- (1) Sutton, A. P.; Balluffi, R. W. *Interfaces in Crystalline Materials*; Clarendon Press: 1995.
- (2) Browning, N. D.; Klie, R. F.; Lei, Y. Vacancy Segregation at Grain Boundaries in Ceramic Oxides. In *Mixed Ionic Electronic Conducting Perovskites for Advanced Energy Systems*; Kluwer: The Netherlands, 2004; pp 15–25.
- (3) Lee, W.; Jung, H. J.; Lee, M. H.; Kim, Y.-B.; Park, J. S.; Sinclair, R.; Prinz, F. B. Oxygen Surface Exchange at Grain Boundaries of Oxide Ion Conductors. *Adv. Funct. Mater.* **2012**, *22* (5), 965–971.
- (4) Ye, F.; Yin, C. Y.; Ou, D. R.; Mori, T. Relationship between Lattice Mismatch and Ionic Conduction of Grain Boundary in YSZ. *Prog. Nat. Sci.* **2014**, *24* (1), 83–86.
- (5) Bowman, W. J.; Zhu, J.; Sharma, R.; Crozier, P. A. Electrical Conductivity and Grain Boundary Composition of Gd-Doped and Gd/Pr Co-Doped Ceria. *Solid State Ionics* **2015**, *272*, 9–17.
- (6) Lin, Y.; Fang, S.; Su, D.; Brinkman, K. S.; Chen, F. Enhancing Grain Boundary Ionic Conductivity in Mixed Ionic–Electronic Conductors. *Nat. Commun.* **2015**, *6*, 6824–6833.
- (7) Nafsin, N.; Aguiar, J. A.; Aoki, T.; Thron, A.; van Benthem, K.; Castro, R. H. R. Thermodynamics versus Kinetics of Grain Growth Control in Nanocrystalline Zirconia. *Acta Mater.* **2017**, *136*, 224–234.
- (8) Feng, B.; Lugg, N. R.; Kumamoto, A.; Ikuhara, Y.; Shibata, N. Direct Observation of Oxygen Vacancy Distribution across Yttria-Stabilized Zirconia Grain Boundaries. *ACS Nano* **2017**, *11*, 11376–11382.
- (9) Bowman, W. J.; Kelly, M. N.; Rohrer, G. S.; Hernandez, C. A.; Crozier, P. A. Enhanced Ionic Conductivity in Electroceramics by Nanoscale Enrichment of Grain Boundaries with High Solute Concentration. *Nanoscale* **2017**, *9*, 17293–17302.
- (10) Ma, C.; Chen, K.; Liang, C.; Nan, C.-W.; Ishikawa, R.; More, K.; Chi, M. Atomic-Scale Origin of the Large Grain-Boundary Resistance in Perovskite Li-Ion-Conducting Solid Electrolytes. *Energy Environ. Sci.* **2014**, *7* (5), 1638–1642.

- (11) Yu, S.; Siegel, D. J. Grain Boundary Contributions to Li-Ion Transport in the Solid Electrolyte $\text{Li}^{\text{+}}\text{La}_3\text{Zr}_2\text{O}_{12}$ (LLZO). *Chem. Mater.* **2017**, *29* (22), 9639–9647.
- (12) Lotsch, B. V.; Maier, J. Relevance of Solid Electrolytes for Lithium-Based Batteries: A Realistic View. *J. Electroceram.* **2017**, *38* (2), 128–141.
- (13) Guo, X.; Maier, J. Grain Boundary Blocking Effect in Zirconia: A Schottky Barrier Analysis. *J. Electrochem. Soc.* **2001**, *148* (3), E121–E126.
- (14) Avila-Paredes, H. J.; Choi, K.; Chen, C.-T.; Kim, S. Dopant-Concentration Dependence of Grain-Boundary Conductivity in Ceria: A Space-Charge Analysis. *J. Mater. Chem.* **2009**, *19* (27), 4837–4842.
- (15) Tuller, H. L.; Bishop, S. R. Point Defects in Oxides: Tailoring Materials Through Defect Engineering. *Annu. Rev. Mater. Res.* **2011**, *41* (1), 369–398.
- (16) Wang, D. Y.; Nowick, A. S. The “Grain-Boundary Effect” in Doped Ceria Solid Electrolytes. *J. Solid State Chem.* **1980**, *35* (3), 325–333.
- (17) Gerhardt, R.; Nowick, A. S.; Mochel, M. E.; Dumler, I. Grain-Boundary Effect in Ceria Doped with Trivalent Cations: II, Microstructure and Microanalysis. *J. Am. Ceram. Soc.* **1986**, *69* (9), 647–651.
- (18) Guo, X.; Sigle, W.; Maier, J. Blocking Grain Boundaries in Yttria-Doped and Undoped Ceria Ceramics of High Purity. *J. Am. Ceram. Soc.* **2003**, *86* (1), 77–87.
- (19) Avila-Paredes, H. J.; Kim, S. The Effect of Segregated Transition Metal Ions on the Grain Boundary Resistivity of Gadolinium Doped Ceria: Alteration of the Space Charge Potential. *Solid State Ionics* **2006**, *177* (35–36), 3075–3080.
- (20) Jasper, A.; Kilner, J. A.; McComb, D. W. TEM and Impedance Spectroscopy of Doped Ceria Electrolytes. *Solid State Ionics* **2008**, *179* (21–26), 904–908.
- (21) Mebane, D. S.; De Souza, R. A. A Generalised Space-Charge Theory for Extended Defects in Oxygen-Ion Conducting Electrolytes: From Dilute to Concentrated Solid Solutions. *Energy Environ. Sci.* **2015**, *8* (10), 2935–2940.
- (22) Cheng, E. J.; Sharafi, A.; Sakamoto, J. Intergranular Li Metal Propagation through Polycrystalline $\text{Li}^{+}\text{6.25Al}_2\text{O}_5\text{La}_3\text{Zr}_2\text{O}_{12}$ Ceramic Electrolyte. *Electrochim. Acta* **2017**, *223*, 85–91.
- (23) Shibata, N.; Findlay, S. D.; Azuma, S.; Mizoguchi, T.; Yamamoto, T.; Ikuhara, Y. Atomic-Scale Imaging of Individual Dopant Atoms in a Buried Interface. *Nat. Mater.* **2009**, *8* (8), 654–658.
- (24) An, J.; Park, J. S.; Koh, A. L.; Lee, H. B.; Jung, H. J.; Schoonman, J.; Sinclair, R.; Gür, T. M.; Prinz, F. B. Atomic Scale Verification of Oxide-Ion Vacancy Distribution near a Single Grain Boundary in YSZ. *Sci. Rep.* **2013**, *3*, 2680–2686.
- (25) Shibata, N.; Oba, F.; Yamamoto, T.; Ikuhara, Y. Structure, Energy and Solute Segregation Behaviour of [110] Symmetric Tilt Grain Boundaries in Yttria-Stabilized Cubic Zirconia. *Philos. Mag.* **2004**, *84* (23), 2381–2415.
- (26) Lee, H. B.; Prinz, F. B.; Cai, W. Atomistic Simulations of Grain Boundary Segregation in Nanocrystalline Yttria-Stabilized Zirconia and Gadolinia-Doped Ceria Solid Oxide Electrolytes. *Acta Mater.* **2013**, *61* (10), 3872–3887.
- (27) Tong, W.; Yang, H.; Moeck, P.; Nandasiri, M. I.; Browning, N. D. General Schema for [001] Tilt Grain Boundaries in Dense Packing Cubic Crystals. *Acta Mater.* **2013**, *61* (9), 3392–3398.
- (28) Cantwell, P. R.; Tang, M.; Dillon, S. J.; Luo, J.; Rohrer, G. S.; Harmer, M. P. Grain Boundary Complexions. *Acta Mater.* **2014**, *62*, 1–48.
- (29) Diercks, D. R.; Tong, J.; Zhu, H.; Kee, R.; Baure, G.; Nino, J. C.; O’Hayre, R.; Gorman, B. P. Three-Dimensional Quantification of Composition and Electrostatic Potential at Individual Grain Boundaries in Doped Ceria. *J. Mater. Chem. A* **2016**, *4* (14), 5167–5175.
- (30) Aoki, M.; Chiang, Y.-M.; Kosacki, I.; Lee, L. J.-R.; Tuller, H. L.; Liu, Y. Solute Segregation and Grain-Boundary Impedance in High-Purity Stabilized Zirconia. *J. Am. Ceram. Soc.* **1996**, *79* (5), 1169–1180.
- (31) Zhang, T.; Zeng, Z.; Huang, H.; Hing, P.; Kilner, J. Effect of Alumina Addition on the Electrical and Mechanical Properties of $\text{Ce}_0.8\text{Gd}_0.2\text{O}_{2-\delta}$ Ceramics. *Mater. Lett.* **2002**, *57* (1), 124–129.
- (32) Tschöpe, A.; Sommer, E.; Birringer, R. Grain Size-Dependent Electrical Conductivity of Polycrystalline Cerium Oxide: I. *Solid State Ionics* **2001**, *139* (3), 255–265.
- (33) Tschöpe, A. Grain Size-Dependent Electrical Conductivity of Polycrystalline Cerium Oxide II: Space Charge Model. *Solid State Ionics* **2001**, *139* (3), 267–280.
- (34) Tschöpe, A.; Kilassonia, S.; Birringer, R. The Grain Boundary Effect in Heavily Doped Cerium Oxide. *Solid State Ionics* **2004**, *173* (1–4), 57–61.
- (35) De Souza, R. A.; Munir, Z. A.; Kim, S.; Martin, M. Defect Chemistry of Grain Boundaries in Proton-Conducting Solid Oxides. *Solid State Ionics* **2011**, *196* (1), 1–8.
- (36) Shirpour, M.; Rahmati, B.; Sigle, W.; van Aken, P. A.; Merkle, R.; Maier, J. Dopant Segregation and Space Charge Effects in Proton-Conducting BaZrO_3 Perovskites. *J. Phys. Chem. C* **2012**, *116* (3), 2453–2461.
- (37) Joakim Nyman, B.; Helgee, E. E.; Wahnström, G. Oxygen Vacancy Segregation and Space-Charge Effects in Grain Boundaries of Dry and Hydrated BaZrO_3 . *Appl. Phys. Lett.* **2012**, *100* (6), No. 061903.
- (38) Litzelman, S. J.; De Souza, R. A.; Butz, B.; Tuller, H. L.; Martin, M.; Gerthsen, D. Heterogeneously Doped Nanocrystalline Ceria Films by Grain Boundary Diffusion: Impact on Transport Properties. *J. Electroceram.* **2009**, *22* (4), 405–415.
- (39) Mills, E. M.; Kleine-Boymann, M.; Janek, J.; Yang, H.; Browning, N. D.; Takamura, Y.; Kim, S. YSZ Thin Films with Minimized Grain Boundary Resistivity. *Phys. Chem. Chem. Phys.* **2016**, *18* (15), 10486–10491.
- (40) Navickas, E.; Chen, Y.; Lu, Q.; Wallisch, W.; Huber, T. M.; Bernardi, J.; Stöger-Pollach, M.; Friedbacher, G.; Hutter, H.; Yildiz, B.; et al. Dislocations Accelerate Oxygen Ion Diffusion in $\text{La}^{0.8}\text{Sr}^{0.2}\text{MnO}_3$ Epitaxial Thin Films. *ACS Nano* **2017**, *11* (11), 11475–11487.
- (41) Polfus, J. M.; Yildiz, B.; Tuller, H. L. Origin of Fast Oxide Ion Diffusion along Grain Boundaries in Sr-Doped LaMnO_3 . *Phys. Chem. Chem. Phys.* **2018**, *20* (28), 19142–19150.
- (42) Sun, L.; Marrocchelli, D.; Yildiz, B. Edge Dislocation Slows down Oxide Ion Diffusion in Doped CeO_2 by Segregation of Charged Defects. *Nat. Commun.* **2015**, *6*, 6294.
- (43) Fleig, J.; Rodewald, S.; Maier, J. Microcontact Impedance Measurements of Individual Highly Resistive Grain Boundaries: General Aspects and Application to Acceptor-Doped SrTiO_3 . *J. Appl. Phys.* **2000**, *87* (5), 2372–2381.
- (44) De Souza, R. A.; Fleig, J.; Maier, J.; Zhang, Z.; Sigle, W.; Rühle, M. Electrical Resistance of Low-Angle Tilt Grain Boundaries in Acceptor-Doped SrTiO_3 as a Function of Misorientation Angle. *J. Appl. Phys.* **2005**, *97* (5), No. 053502.
- (45) Zhang, Z.; Sigle, W.; De Souza, R. A.; Kurtz, W.; Maier, J.; Rühle, M. Comparative Studies of Microstructure and Impedance of Small-Angle Symmetrical and Asymmetrical Grain Boundaries in SrTiO_3 . *Acta Mater.* **2005**, *53* (19), 5007–5015.
- (46) McNealy, B. E.; Hertz, J. L. On the Use of the Constant Phase Element to Understand Variation in Grain Boundary Properties. *Solid State Ionics* **2014**, *256*, 52–60.
- (47) Shirpour, M.; Gregori, G.; Houben, L.; Merkle, R.; Maier, J. High Spatially Resolved Cation Concentration Profile at the Grain Boundaries of Sc-Doped BaZrO_3 . *Solid State Ionics* **2014**, *262*, 860–864.
- (48) Andersson, D. A.; Simak, S. I.; Skorodumova, N. V.; Abrikosov, I. A.; Johansson, B. Optimization of Ionic Conductivity in Doped Ceria. *Proc. Natl. Acad. Sci. U. S. A.* **2006**, *103* (10), 3518–3521.
- (49) Dholabhai, P. P.; Adams, J. B.; Crozier, P. A.; Sharma, R. In Search of Enhanced Electrolyte Materials: A Case Study of Doubly Doped Ceria. *J. Mater. Chem.* **2011**, *21* (47), 18991–18997.

- (50) Darbal, A. D.; Ganesh, K. J.; Liu, X.; Lee, S.-B.; Ledonne, J.; Sun, T.; Yao, B.; Warren, A. P.; Rohrer, G. S.; Rollett, A. D.; et al. Grain Boundary Character Distribution of Nanocrystalline Cu Thin Films Using Stereological Analysis of Transmission Electron Microscope Orientation Maps. *Microsc. Microanal.* **2013**, *19* (01), 111–119.
- (51) Aebersold, A. B.; Alexander, D. T. L.; Hébert, C. Height-Resolved Quantification of Microstructure and Texture in Polycrystalline Thin Films Using TEM Orientation Mapping. *Ultramicroscopy* **2015**, *159*, 112–123.
- (52) Mackenzie, J. K. Second Paper on Statistics Associated with the Random Disorientation of Cubes. *Biometrika* **1958**, *45* (1/2), 229–240.
- (53) Helmick, L.; Dillon, S. J.; Gerdes, K.; Gemmen, R.; Rohrer, G. S.; Seetharaman, S.; Salvador, P. A. Crystallographic Characteristics of Grain Boundaries in Dense Yttria-Stabilized Zirconia. *Int. J. Appl. Ceram. Technol.* **2011**, *8* (5), 1218–1228.
- (54) Shannon, R. D. Revised Effective Ionic Radii and Systematic Studies of Interatomic Distances in Halides and Chalcogenides. *Acta Crystallogr., Sect. A: Cryst. Phys., Diff., Theor. Gen. Crystallogr.* **1976**, *32* (5), 751–767.
- (55) Nafsin, N.; Castro, R. H. R. Direct measurements of quasi-zero grain boundary energies in ceramics. *J. Mater. Res.* **2017**, *32* (1), 166–173.
- (56) Saylor, D. M.; Morawiec, A.; Adams, B. L.; Rohrer, G. S. Misorientation Dependence of the Grain Boundary Energy in Magnesia. *Interface Sci.* **2000**, *8* (2–3), 131–140.
- (57) Aidhy, D. S.; Zhang, Y.; Weber, W. J. Impact of Segregation Energetics on Oxygen Conductivity at Ionic Grain Boundaries. *J. Mater. Chem. A* **2014**, *2* (6), 1704–1709.
- (58) Arora, G.; Aidhy, D. S. Segregation and Binding Energetics at Grain Boundaries in Fluorite Oxides. *J. Mater. Chem. A* **2017**, *5* (8), 4026–4035.
- (59) Bowman, W. J.; March, K.; Hernandez, C. A.; Crozier, P. A. Measuring Bandgap States in Individual Non-Stoichiometric Oxide Nanoparticles Using Monochromated STEM EELS: The Praseodymium–Ceria Case. *Ultramicroscopy* **2016**, *167*, 5–10.
- (60) Gerhardt, R.; Nowick, A. S. Grain-Boundary Effect in Ceria Doped with Trivalent Cations: I, Electrical Measurements. *J. Am. Ceram. Soc.* **1986**, *69* (9), 641–646.
- (61) Christie, G. M.; van Berkel, F. P. F. Microstructure-Ionic Conductivity Relationships in Ceria-Gadolinia Electrolytes. *Solid State Ionics* **1996**, *83*, 17–27.
- (62) Zhang, T. S.; Ma, J.; Cheng, H.; Chan, S. H. Ionic Conductivity of High-Purity Gd-Doped Ceria Solid Solutions. *Mater. Res. Bull.* **2006**, *41* (3), 563–568.
- (63) Lei, Y.; Ito, Y.; Browning, N. D.; Mazanec, T. J. Segregation Effects at Grain Boundaries in Fluorite-Structured Ceramics. *J. Am. Ceram. Soc.* **2002**, *85* (9), 2359–2363.
- (64) Li, F.; Ohkubo, T.; Chen, Y. M.; Kodzuka, M.; Ye, F.; Ou, D. R.; Mori, T.; Hono, K. Laser-Assisted Three-Dimensional Atom Probe Analysis of Dopant Distribution in Gd-Doped CeO₂. *Scr. Mater.* **2010**, *63* (3), 332–335.
- (65) Vikrant, K. S. N.; Chueh, W. C.; García, R. E. Charged Interfaces: Electrochemical and Mechanical Effects. *Energy Environ. Sci.* **2018**, *11* (8), 1993–2000.
- (66) Wells, D. B.; Stewart, J.; Herbert, A. W.; Scott, P. M.; Williams, D. E. The Use of Percolation Theory to Predict the Probability of Failure of Sensitized, Austenitic Stainless Steels by Intergranular Stress Corrosion Cracking. *Corrosion* **1989**, *45* (8), 649–660.
- (67) Manoubi, T.; Colliex, C.; Rez, P. Quantitative Electron Energy Loss Spectroscopy on M₄₅ Edges in Rare Earth Oxides. *J. Electron Spectrosc. Relat. Phenom.* **1990**, *50*, 1–18.
- (68) Egerton, R. F. Factors Affecting the Accuracy of Elemental Analysis by Transmission EELS. *Microsc., Microanal., Microstruct.* **1991**, *2* (2–3), 203–213.

**Linking macroscopic and nanoscopic ionic conductivity:
A semi-empirical framework for characterizing grain boundary conductivity in
polycrystalline ceramics**

Supporting Information

William J. Bowman^{1+}, Amith Darbal² and Peter A. Crozier^{1*}*

1. School for Engineering of Matter, Transport and Energy,
Arizona State University, 501 E. Tyler Mall, Tempe, AZ 85287-6106, USA
2. Nanomegas USA, 1095 W. Rio Salado Pkwy #110, Tempe, AZ 85281, USA

+ Present Address: Department of Materials Science and Engineering,
University of California, Irvine

* E-mail: crozier@asu.edu, will.bowman@uci.edu

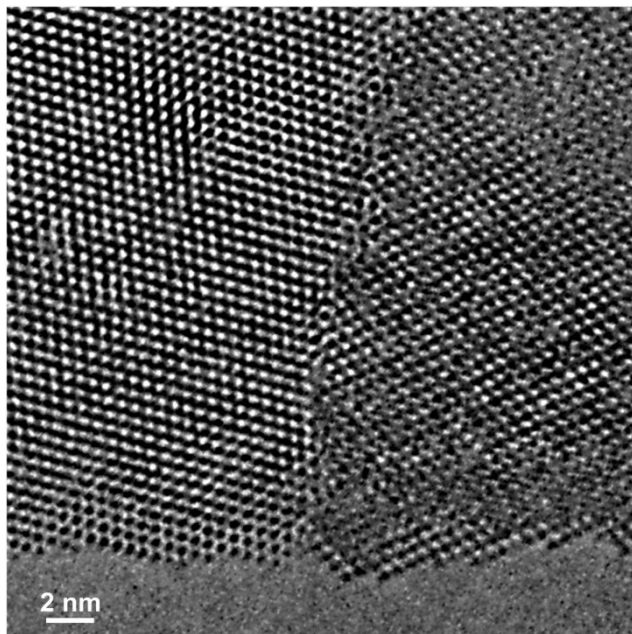


Figure S1 | Intergranular amorphous phases were not observed using high resolution imaging. Bright field TEM image of a typical GB in $\text{Pr}_{0.04}\text{Gd}_{0.11}\text{Ce}_{0.85}\text{O}_{2-\delta}$; there was no evidence for the formation of amorphous intergranular phases in this material.¹

Coincident site lattice type boundaries

Figure S2 shows the length fraction of various coincidence site lattice (CSL) GBs, where the angle-axis relationship of adjacent grains is such that their lattice sites coincide partially.^{2,3} Though $\Sigma 3$ -type GBs are the most prevalent, representing about 6 % of the total length, only about 23 % of the total length was associated with CSL-type GBs. This suggests that in this case, high spatial resolution studies should focus predominantly on *non CSL-type* boundaries if they are to be more applicable to polycrystalline materials with random grain orientation.

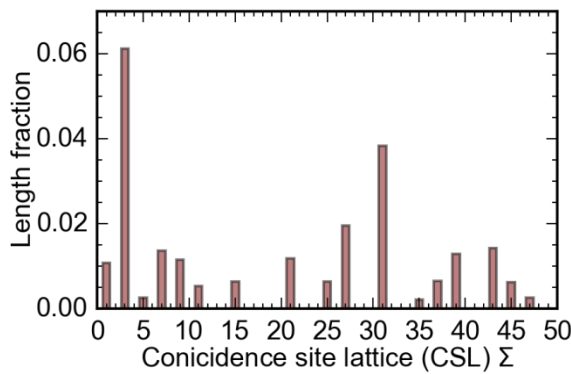


Figure S2 | Coincident-site lattice type grain boundaries comprised only 23% of the total grain boundary length. Length fraction distribution of coincidence site lattice (CSL) grain boundaries.

Table S1 | Parameters used for EELS data fitting and quantification.

EELS edge	Background fitting procedure	Background fitting window(s) [eV]	Signal integration window [eV]	k-factor
Ce M ₄₅	Inverse power-law extrapolation	790 – 875	875 – 915	
Pr M ₄₅	Two-window inverse power-law interpolation	920 – 925, 1150 – 1170	925 – 970	$k_{PrCe} = 1.39$
Gd M ₄₅	Inverse power-law extrapolation	1120 – 1180	1180 – 1230	$k_{GdCe} = 2.12$

Comparing correlated approach with random GB sampling

To map GB length fraction to GB solute concentration, and to generalize locally-measured GB composition the entire GB population, GB composition distributions (Figure 3a) were fit with a linear function of misorientation angle (see Table 1 for fitting parameters). These functions were related to the misorientation angle distribution (MAD, Figure 1c) via misorientation angle, yielding the so-called *concentration length fraction distribution* (CLFD), which describes the length fraction of GBs with a particular cation concentration. **Figure S3** presents the PGCO CLFD, with GBs binned per their cation concentration. The CLFD for each cation is peaked and skewed slightly, resembling the MAD (Figure 1c). This approach yields a significant improvement in the understanding of the variation in GB composition compared to analysis of randomly-sampled GBs—which assumes a normal distribution in the solute concentration of GBs in a material. Random sampling omits any influence of GB character on composition, and predicts a symmetric CLFD (or pseudo-symmetric, depending on the composition range used for binning). For comparison, CLFDs generated assuming a normal distribution are overlaid in **Figure S3**, with mean values and standard deviations in provided Table 1.

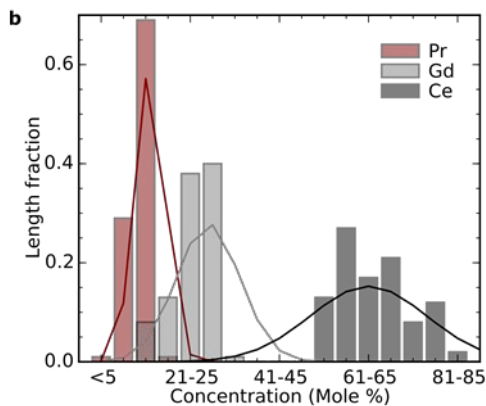


Figure S3 | The new correlated approach improves our understanding of the variation in grain boundary composition compared to conventional random sampling. Length fraction distributions indicating the GB cation concentrations derived by new correlated analysis

(bar charts) and conventional random GB sampling assuming normal distribution of GB composition (solid curves).

The effective grain boundary trivalent solute concentration

The effective GB trivalent solute concentration, $[A^{3+}]_{GB}$, is defined as $[A^{3+}]_{GB} = [Gd^{3+}]_{GB} + [Pr^{3+}]_{GB}$ (Figure S4). The concentration of trivalent praseodymium is assumed to be half of the total praseodymium concentration measured using EELS; because Pr is a minor solute in this case, the exact concentration of trivalent Pr does not strongly influence the result.

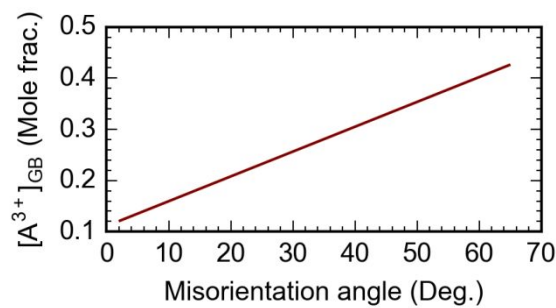


Figure S4 | The effective grain boundary trivalent solute concentration was determined by correlating the measured grain boundary character and composition.

Relating GB migration activation energy and solute concentration

As described in the main text (see Equation 2 and Figure 4a) we determined an empirical relationship between E^{GB} and $[A^{3+}]_{GB}$ for $Gd_xCe_{1-x}O_{2-\delta}$, which allowed us to estimate the GB migration activation energy from GB solute concentration measured using STEM EELS. Unfortunately, these quantities are seldom reported together (e.g. ^{1,4}), but have each been reported individually as a function of nominal solute concentration, $[A^{3+}]_{Nominal}$. For instance, Figure S5 plots published *local* GB solute concentration (measured or simulated) as a function of the *nominal* solute concentration in $Gd_xCe_{1-x}O_{2-\delta}$. The literature data were parameterized using Equation (S1), which is plotted with the data below.

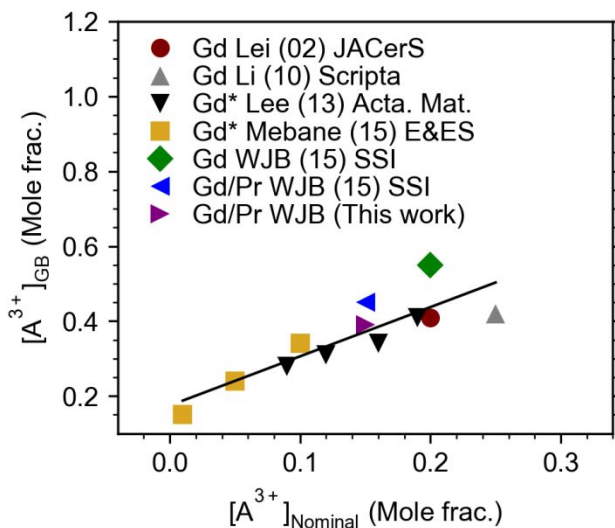


Figure S5 | Published grain boundary solute composition data were collected to correlate composition and migration activation energy. Measured or simulated (simulated values are labelled with * in legend) GB solute concentration, $[A^{3+}]_{GB}$, plotted as a function of nominal solute concentration, $[A^{3+}]_{Nominal}$, in $Gd_xCe_{1-x}O_{2-\delta}$.^{1,5-9} Reprinted in part with permission from Supporting Information ref. 1; copyright 2014 Elsevier B.V. Reprinted in part with permission from Supporting Information ref. 5; copyright 2004 John Wiley and Sons. Reprinted in part with permission from Supporting Information ref. 6; copyright 2010 Acta Materialia Inc. Reprinted in part with permission from Supporting Information ref. 7; copyright 2012 John Wiley and Sons. Reprinted in part with permission from Supporting Information ref. 8; copyright 2010 Acta Materialia Inc. Reprinted in part with permission from Supporting Information ref. 9; copyright 2015 The Royal Society of Chemistry.

$$[A^{3+}]_{GB} = 1.31 \cdot [A^{3+}]_{Nominal} + 0.17 \quad (S1)$$

Choosing a function to fit E^{GB} vs. $[A^{3+}]_{GB}$ from literature

The smooth function used to fit the literature data of GB migration activation energy vs. GB solute concentration has a direct impact on the GB property distributions, e.g. the activation energy and GB conductivity distributions (Figure 4b and Figure 4c). We tested three alternative fitting functions, so-called “Decaying Exponential” (Equation 2 and Figure 4a in the main text, Table S2 and Figure S6), “Gentle Minimum”, and “U-Shape” (Table S3 and Figure S6), which produced qualitatively similar activation energy and GB conductivity distributions to the fit selecting for the main text (black curve in Figure 4).

Table S2 | Coefficients of Equation (2), $E^{GB} = a \cdot ([A^{3+}]_{GB})^r + c$ (“Decaying Exponential”).

	a	r	c
Minimum fit (red curve, Figure S6)	$1.6 \cdot 10^{-4}$	-4	0.91
Medium fit (black curve, Figure 4a and Figure S6)	$2 \cdot 10^{-4}$	-5	0.91
Maximum fit (blue curve, Figure S6)	$20 \cdot 10^{-4}$	-4	0.91

The Decaying Exponential model does not capture the local minimum in E^{GB} vs. $[A^{3+}]_{GB}$ around $[A^{3+}]_{GB} = 0.3$, so the Gentle Minimum model was tested (Table S3 and Figure S6), though it showed qualitatively similar results.

Table S3 | Coefficients of $E^{GB} = a \cdot ([A^{3+}]_{GB})^r + b \cdot ([A^{3+}]_{GB})^s + c$ (“Gentle Minimum” and “U-Shape”).

	a	r	b	s	c
Gentle Minimum (green curve, Figure S6)	$2 \cdot 10^{-6}$	-8	2	0.1	0.9
U-Shape (green curve, Figure S6)	0.155	-1.7	307	$5.9 \cdot 10^{-3}$	305

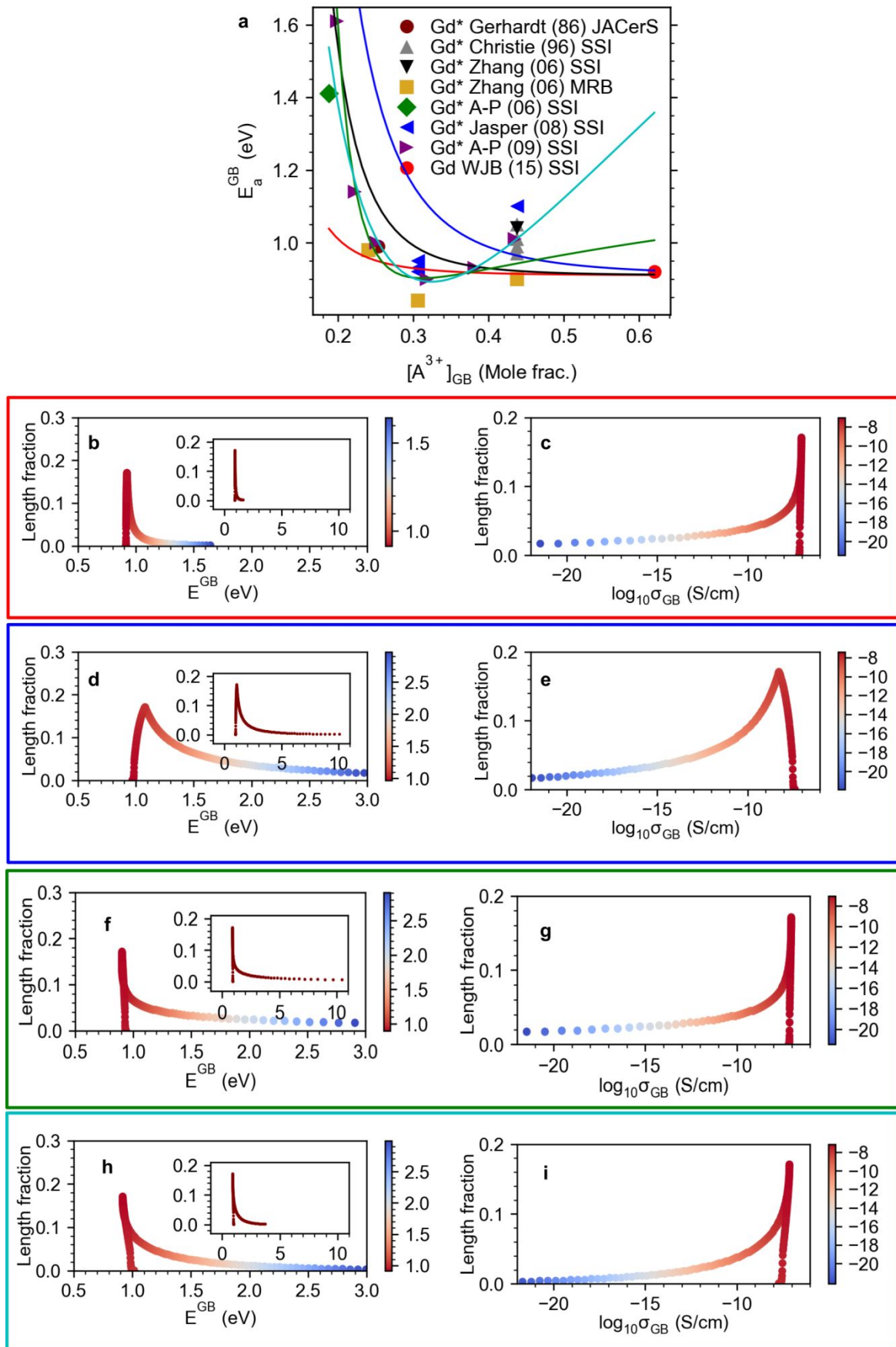


Figure S6 | Varying the fit of the literature data does not sacrifice qualitative aspects of the activation energy and GB conductivity distributions. a, As is the main text Figure 4a, literature data showing the relationship between E^{GB} and $[A^{3+}]_{GB}$ (measured directly or calculated using Equation (S1)) for comparable $Gd_xCe_{1-x}O_{2-\delta}$ solid solutions. The data are fit using two different functions: The “Decaying Exponential” described by Equation (2) (black) with enveloping fits (blue and red) were created by varying the coefficients of Equation (2) to account for the data scatter, and the “Gentle Minimum” (green) and “U-Shape” (cyan) fits by the function detailed in Table S3. The legend indicates the solute species, and if the data were measured directly (i.e. only “Gd WJB (15) SSI”) or estimated (labelled with * if estimated; see Figure S5). b-e, Activation energy and GB conductivity distributions determined using minimum (b,c) and maximum (d,e) enveloping fits for Decaying Exponential model. (f,g) Activation energy and GB conductivity distributions determined using Gentle Minimum model. (h,i) Activation energy and GB conductivity distributions determined using U-Shape model.

Predicting solute segregation using the Gouy-Chapman model

An expression relating the space charge potential (SCP) and the concentration of a charged defect, j , at a distance x from the grain boundary is derived below.^{10,11} The electrochemical potential of a species j , $\tilde{\mu}_j$, is defined in Equation (S2), where μ_j^0 is the standard chemical potential, a the activity, and ϕ the electrostatic potential.

$$\tilde{\mu}_j = \mu_j^0 + kT\ln a_j + z_j e\phi \quad (\text{S2})$$

Under thermodynamic equilibrium, the electrochemical potential of j is assumed to be constant at any two points x_1 and x_2 .

$$\tilde{\mu}_j(x_1) = \tilde{\mu}_j(x_2) \quad (\text{S3})$$

When the concentration of j is assumed to be dilute, i.e. they are non-interacting point defects, activity can be approximated as the molar concentration (or site fraction), n .¹² Under this assumption, substitution of Equation (S2) into Equation (S3) yields

$$\mu_j^0(x_1) + kT\ln n_j(x_1) + z_j e\phi(x_1) = \mu_j^0(x_2) + kT\ln n_j(x_2) + z_j e\phi(x_2) \quad (\text{S4})$$

which simplifies to

$$\ln n_j(x_1) - \ln n_j(x_2) = \frac{z_j e}{kT}(\phi(x_2) - \phi(x_1)) \quad (\text{S5})$$

(The non-interacting defect approximation which permits replacement of activities with concentration is a key assumption underlying the Mott Schottky and Gouy Chapman models. It breaks down for grain boundaries solute concentrations of greater than 10%,⁹ which is typical of

the observations reported here). Taking x_2 to be located some distance away from the grain boundary in the neutral grain, $n_j(x_2)$ can be approximated as the nominal bulk concentration of j , n_j^{Bulk} , and Equation (S5) can be expressed as

$$\frac{n_j(x_1)}{n_j^{Bulk}} = \exp\left(-\frac{z_j e}{kT} \Delta\phi\right) \quad (\text{S6})$$

where $\Delta\phi$ is the grain boundary SCP if x_1 is taken to be the position of the boundary mid-plane.

Two solutions to Equation (S6) yield (i) the so-called Mott-Schottky condition, whereby the acceptor concentration is assumed to be fixed at all locations in the space charge region, which may be a reasonable assumption depending on the thermal history of the material containing said space charge region. And (ii) the Gouy-Chapman condition whereby the acceptor concentration can vary spatially, resembling the segregation behavior commonly observed in oxides that have undergone high temperature processing such as sintering. (For graphical comparison see Figure 4 of Ref. ¹¹.)

Below we apply the Gouy-Chapman model to simulate the variability in GB solute segregation observed experimentally and the associated space charge potential. As shown for a planar grain boundary by Tschöpe and Birringer,¹³ a defect's concentration at a distance x from the GB, $C(x)$, is related to the SCP, $\Delta\phi$, via Equations (S7) and (S8).

$$\frac{C(x)}{C_{Bulk}} = \left(\frac{1 + \theta \cdot \exp(-x/\lambda)}{1 - \theta \cdot \exp(-x/\lambda)} \right)^{2Z} \quad (\text{S7})$$

$$\theta = \tanh\left(\frac{ze\Delta\phi}{4kT}\right) \quad (\text{S8})$$

where C_{Bulk} is the nominal solute concentration, λ the Debye length, θ the profile parameter, z the point defect's charge relative to the host, k the Boltzmann constant, and T the temperature.

Figure S7a presents the spatial variation of $C(x)$ calculated using Equation (S7) for several combinations of $\Delta\phi$ and T which yield trivalent solute concentration profiles comparable to those measured here using STEM EELS. λ in this case was taken to be 1.5 nm, which is consistent with values reported for ceria solid solutions, e.g. Ref. ¹⁴. Figure S7b shows the space charge potential as a function of GB solute concentration (at the core). This shows that the SCP *increases* with increasing solute segregation. Within this model, increasing space charge potential decreases the carrier concentration and decreases the grain boundary conductivity, which contradicts the experimental observations. The origin of the problem is that the conductivity depends on the product of the carrier concentration and the mobility. The mobility depends exponentially on the grain boundary migration activation energy which decreases with increasing solute concentration (Figure 4a) causing the mobility to increase. The variation in mobility with solute concentration is lost when the activity is replaced with concentration in the derivation of Equation (S4).

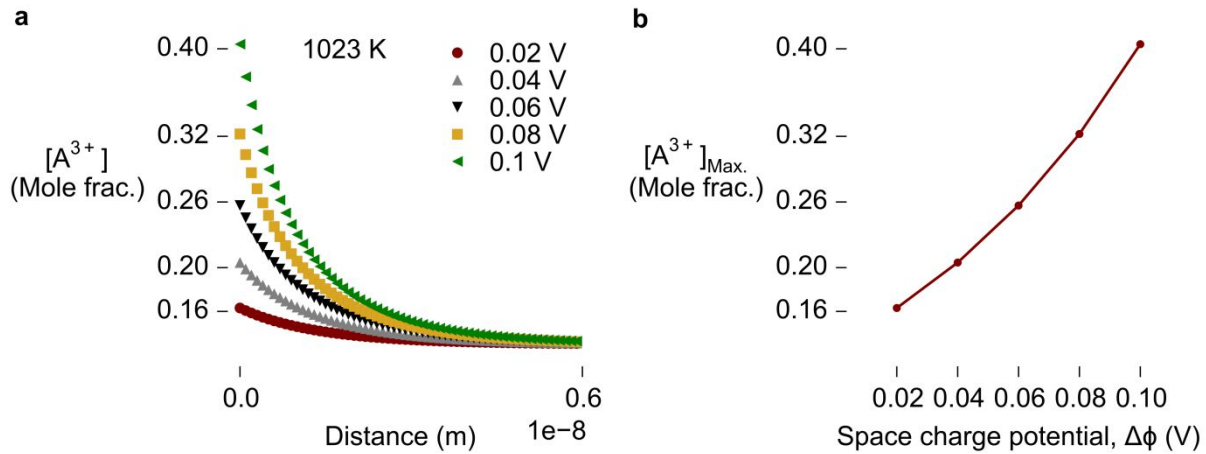


Figure S7 | The Gouy-Chapman model for solute segregation does not describe the measurements reported here. a, Trivalent solute concentration profiles calculated using the Gouy-Chapman model (Equation (S7)) with various values of space charge potential, $\Delta\phi$. b, Maxima of the profiles in a.

Derivation of model for grain boundary conductivity distribution

The conductivity of a mobile charge carrier of species i which undergoes thermally-activated migration in the presence of an electrical field, e.g. an oxygen ion/vacancy, can be expressed using Equation (S9), where σ_i is the conductivity, β_i the carrier-concentration-independent pre-exponential factor, n_i the carrier concentration, and E_i the carrier migration activation energy.¹⁵

$$\sigma_i = \beta_i \frac{n_i}{T} \exp\left(\frac{-E_i}{kT}\right) \quad (\text{S9})$$

The overall GB ionic transport properties in a macroscopic polycrystalline electrolyte arise from ions crossing many different grain boundaries. For an i^{th} individual GB, the average ionic conductance, C_i^{GB} , defined using the brick-layer model¹⁶ is given in Equation (S10).

$$C_i^{\text{GB}} = \sigma_i^{\text{GB}} \frac{A_i^{\text{GB}}}{g_i^{\text{GB}}} \quad (\text{S10})$$

σ_i^{GB} is the conductivity of the GB, A_i^{GB} is the cross-sectional GB area, and g_i^{GB} is the average GB thickness (\sim 1-2 nm, see e.g. Figure 2). Correspondingly, the average ionic resistance of an individual GB, R_i^{GB} , is given by Equation (S11).

$$R_i^{GB} = \frac{1}{C_i^{GB}} = \frac{g_i^{GB}}{A_i^{GB} \sigma_i^{GB}} \quad (\text{S11})$$

For ion transport to occur through a material, the ion/vacancy must traverse m GBs, which together have overall GB resistance, R^{GB} , given by Equation (S12).

$$R^{GB} = R_1^{GB} + R_2^{GB} + \dots + R_m^{GB} = \sum_{i=1}^m R_i^{GB} \quad (\text{S12})$$

By inserting Equations (S9) into (S11), the resistance of an individual GB, R_i^{GB} , can be expressed using Equation (S13), where

$$R_i^{GB} = \frac{g_i^{GB}}{A_i^{GB} \beta_{GB} n_i^{GB}} \exp\left(\frac{E_i^{GB}}{kT}\right) \quad (\text{S13})$$

An ion/vacancy percolating a distance L through a material with average grain size G will traverse m GBs, where $m = L/G$. Assuming $g_i = g$ and $G_i = G$, Equations (S12) and (S13) may be combined to yield Equation (S14).

$$R^{GB} = \frac{g}{G^2 \beta_{GB}} \sum_{i=1}^m \frac{1}{n_i^{GB}} \exp\left(\frac{E_i^{GB}}{kT}\right) \quad (\text{S14})$$

Here, we suppose that, *within the path*, there are N GB types, each with different values of n_j^{GB} and E_j^{GB} , and that there is some probability, p_j , representing the probability distribution of these N types of boundaries such that $\sum p_j = 1$. Hence, summing over all GB types for the m GBs traversed (i.e. $p_j \cdot m$ of each type) yields Equation (S15).

$$R^{GB} = \frac{Lg}{G^3 \beta_{GB}} \sum_{j=1}^N \frac{p_j}{n_j^{GB}} \exp\left(\frac{E_j^{GB}}{kT}\right) \quad (\text{S15})$$

According to the brick-layer model, the specific GB conductivity σ_{GB}^\perp —which estimates the average conductivity of an individual GB from macroscopic electrical measurements, can be calculated using Equation (S16).

$$\sigma_{GB}^\perp = \frac{gL}{GAR^{GB}} = \frac{Lg}{G^3 R^{GB}} \quad (S16)$$

Substituting Equation (S15) into (S16) and rearranging gives Equation (S17).

$$T\sigma_{GB}^\perp = \frac{\beta_{GB}}{\sum_{j=1}^N \frac{p_j}{n_j^{GB}} \exp\left(\frac{E_j^{GB}}{kT}\right)} \quad (S17)$$

σ_{GB}^\perp is the effective conductivity of a percolating path consisting of m GBs of N different types. Generally, there are many possible paths for the ion/vacancy travelling between points A and B, but the ion will follow the path of least resistance. To model this, we assume that only paths with $E^{GB} < E_{Max}^{GB}$ are active in ion/vacancy percolation (ignoring for now the effect of n_j^{GB}). This effectively means that only a subset of low-migration-energy grain boundary types participate in oxygen ion transport. We assume that there are many boundaries along each conducting path, and that the relative distribution of GB types along the path is the same as the relative distribution of all GBs in the material. If we assume there are X different types of grain boundary types in the entire sample with probability, d_k . The probability d_k is assumed to be the distribution measured by STEM OIM (Figure 1c). The distribution of the GB population in the entire sample satisfies Equation (S18).

$$\sum_{k=1}^X d_k = 1 \quad (S18)$$

To evaluate Equation (S17), the p_j probabilities can be determined from the experimental d_k probabilities as follows. The N grain boundary types along the conducting path are labelled with the lowest index j being associated with the lowest activation energy, i.e

$$E_j^{GB} < E_{j+1}^{GB} \quad (S19)$$

We also make the following definitions to simplify the algebra: $j = k$ for $j, k < N$, thus

$$E_j^{GB} = E_k^{GB} \quad (S20)$$

The assumption about the equivalence in the relative probabilities can then be expressed simply as

$$\frac{p_j}{p_{j+1}} = \frac{d_j}{d_{j+1}} \quad (S21)$$

From the normalization conditions, we have

$$\sum_{j=1}^N p_j = 1 \text{ and } \sum_{j=1}^N d_j = \gamma \quad (\text{S22})$$

Inspection of these two equations shows that $p_j = d_j/\gamma$. Thus, the distribution of the GB population along a percolating conduction path, p_j , can be derived from knowledge of the distribution of *all* GBs, d_j , measured by STEM OIM (Figure 1c). Assuming the macroscopic GB conductivity measurements probe the GB percolation path with the lowest resistance, it is possible to rewrite Equation (S17) to include d_j and β_{GB} , as in Equation (S23).

$$T\sigma_{GB}^\perp = \frac{\beta_{GB}\gamma}{\sum_{j=1}^N \frac{d_j}{n_j^{GB}} \exp\left(\frac{E_j^{GB}}{kT}\right)} \quad (\text{S23})$$

The quantities p_j and n_j^{GB} (assuming one oxygen vacancy for every two cations) are accessible via STEM OIM (Figure 1c) and EELS (Figure 3a), respectively.

Equation (S23) is very important because it provides an explicit link between the ionic conductivities of individual grain boundaries derived from nanoscopic composition measurements and the grain boundary conductivity measured macroscopically from a polycrystalline sample using techniques like impedance spectroscopy. If the assumption underlying the derivation of Equation (S23) are reasonable, it should be possible to compare the predicted grain boundary conductivity behavior with data from impedance spectroscopy. The sum of exponentials in the denominator of Equation (S23) will be dominated by the higher activation energy terms provided they are well represented in the distribution. Plotting the logarithm of right-hand side of Equation (S23) against inverse temperature should yield a curve with gradient equal to the experimentally-measured GB migration activation energy assuming the appropriate selection of the parameter N . Since the OIM STEM tells us about the total number of grain boundary types present in the sample. Determining N by fitting to conductivity measured using impedance spectroscopy should provide information on the percolation threshold.

Demonstrating the predictive capability of the model

The predictive capability of the GB transport model based on the correlated TEM approach was demonstrated by applying it to a hypothetical oxide with a lower GB solute concentration but a similar dependence on misorientation angle (Figure S8). This reduced-GB-solute-concentration condition produces a GB concentration distribution (Figure S8b) which is shifted to lower values relative to the high-concentration case shown in Figure 4. Compared to the high-concentration case, the corresponding GB migration activation energy (Figure S8c) and GB ionic conductivity (Figure S8d) distributions are shifted to higher and lower values, respectively. This results in a decrease in predicted ionic conductivity of nearly four orders of magnitude (Figure S8e). In this

case, the conducting fraction of 0.23 (i.e. at the percolation threshold) corresponds to E_{Macro}^{GB} of 1.52 eV (Figure S8f) and predicted E_{Macro}^{GB} of 1.48 eV.

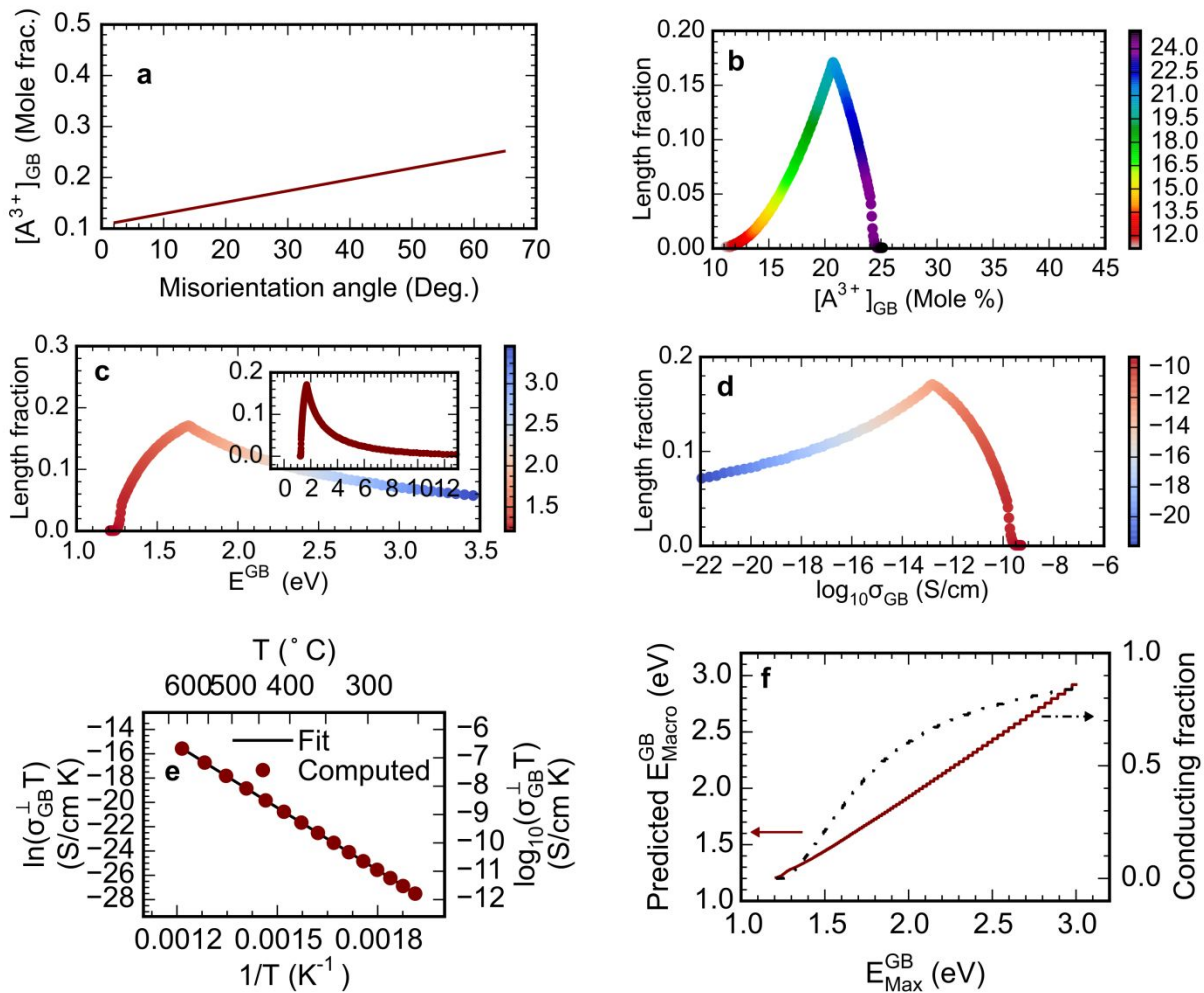


Figure S8 | The grain boundary transport distributions were modulated by modifying the effective grain boundary trivalent solute concentration. a, Dependence of effective GB trivalent solute concentration, $[A^{3+}]_{GB}$, on misorientation angle in a hypothetical oxide with weaker solute segregation to grain boundaries. b, Length fraction distribution of $[A^{3+}]_{GB}$ is shifted to lower GB solute concentrations. c and d, The corresponding GB migration activation energy distribution (c) and GB ionic conductivity distribution (c). e, Effective GB ionic conductivity along the percolating path computed using Equation 3, with $E_{Max}^{GB} = 1.52$ eV (corresponding to conducting fraction of 0.23). f, Predicted E_{Macro}^{GB} and conducting fraction for the hypothetical oxide. E_{Max}^{GB} corresponding to conducting fraction of 0.23, the percolation threshold.

Supplemental References

1. Bowman, W. J., Zhu, J., Sharma, R. & Crozier, P. A. Electrical conductivity and grain boundary composition of Gd-doped and Gd/Pr co-doped ceria. *Solid State Ion.* **272**, 9–17 (2015).
2. Brandon, D. G. The Structure of High-Angle Grain Boundaries. *Acta Metall.* **14**, 1479–1484 (1966).
3. King, A. H. & Shekhar, S. What does it mean to be special? The significance and application of the Brandon criterion. *J. Mater. Sci.* **41**, 7675–7682 (2006).
4. Bowman, W. J., Kelly, M. N., Rohrer, G. S., Hernandez, C. A. & Crozier, P. A. Enhanced ionic conductivity in electroceramics by nanoscale enrichment of grain boundaries with high solute concentration. *Nanoscale* **9**, 17293–17302 (2017).
5. Lei, Y., Ito, Y., Browning, N. D. & Mazanec, T. J. Segregation Effects at Grain Boundaries in Fluorite-Structured Ceramics. *J. Am. Ceram. Soc.* **85**, 2359–2363 (2002).
6. Li, F. *et al.* Laser-assisted three-dimensional atom probe analysis of dopant distribution in Gd-doped CeO₂. *Scr. Mater.* **63**, 332–335 (2010).

7. Lee, W. *et al.* Oxygen Surface Exchange at Grain Boundaries of Oxide Ion Conductors. *Adv. Funct. Mater.* **22**, 965–971 (2012).
8. Lee, H. B., Prinz, F. B. & Cai, W. Atomistic simulations of grain boundary segregation in nanocrystalline yttria-stabilized zirconia and gadolinia-doped ceria solid oxide electrolytes. *Acta Mater.* **61**, 3872–3887 (2013).
9. Mebane, D. S. & De Souza, R. A. A generalised space-charge theory for extended defects in oxygen-ion conducting electrolytes: from dilute to concentrated solid solutions. *Energy Environ. Sci.* **8**, 2935–2940 (2015).
10. Franceschetti, D. R. Local thermodynamic formalism for space charge in ionic crystals. *Solid State Ion.* **2**, 39–42 (1981).
11. Tuller, H. L. & Bishop, S. R. Point Defects in Oxides: Tailoring Materials Through Defect Engineering. *Annu. Rev. Mater. Res.* **41**, 369–398 (2011).
12. Kröger, F. A. & Vink, H. J. Relationships between the Concentrations of Imperfections in Crystalline Solids. *J. Solid State Phys.* **3**, 307–435 (1956).
13. Tschöpe, A. & Birringer, R. Grain size dependence of electrical conductivity in polycrystalline cerium oxide. *J. Electroceramics* **7**, 169–177 (2001).

14. Diercks, D. R. *et al.* Three-dimensional quantification of composition and electrostatic potential at individual grain boundaries in doped ceria. *J Mater Chem A* **4**, 5167–5175 (2016).
15. Kingery, W. D., Bowen, H. K. & Uhlmann, D. R. *Introduction to Ceramics*. (Wiley-Interscience, 1976).
16. Haile, S. M., West, D. L. & Campbell, J. The role of microstructure and processing on the proton conducting properties of gadolinium-doped barium cerate. *J. Mater. Res.* **13**, 1576–1595 (1998).